

A census of massive stars in NGC 346*

Stellar parameters and rotational velocities

P. L. Dufton¹, C. J. Evans², I. Hunter¹, D. J. Lennon³, and F.R.N. Schneider^{4,5}

¹ Astrophysics Research Centre, School of Mathematics & Physics, The Queen's University of Belfast, Belfast, BT7 1NN, Northern Ireland, UK

² UK Astronomy Technology Centre, Royal Observatory, Blackford Hill, Edinburgh, EH9 3HJ, UK

³ Instituto de Astrofísica de Canarias, E-38205 La Laguna, Tenerife, Spain

⁴ Zentrum für Astronomie der Universität Heidelberg, Astronomisches Rechen-Institut, Mönchhofstr. 12-14, 69120 Heidelberg, Germany

⁵ Heidelberger Institut für Theoretische Studien, Schloss-Wolfsbrunnenweg 35, 69118 Heidelberg, Germany

Received; accepted

ABSTRACT

Spectroscopy for 247 stars towards the young cluster NGC 346 in the Small Magellanic Cloud has been combined with that for 116 targets from the VLT-FLAMES Survey of Massive Stars. Spectral classification yields a sample of 47 O-type and 287 B-type spectra, while radial-velocity variations and/or spectral multiplicity have been used to identify 45 candidate single-lined (SB1) systems, 17 double-lined (SB2) systems, and one triple-lined (SB3) system. Atmospheric parameters (T_{eff} and $\log g$) and projected rotational velocities ($v_e \sin i$) have been estimated using TLUSTY model atmospheres; independent estimates of $v_e \sin i$ were also obtained using a Fourier Transform method. Luminosities have been inferred from stellar apparent magnitudes and used in conjunction with the T_{eff} and $v_e \sin i$ estimates to constrain stellar masses and ages using the BONNSAI package. We find that targets towards the inner region of NGC 346 have higher median masses and projected rotational velocities, together with smaller median ages than the rest of the sample. There appears to be a population of very young targets with ages of less than 2 Myr, which have presumably all formed within the cluster. The more massive targets are found to have lower projected rotational velocities consistent with previous studies. No significant evidence is found for differences with metallicity in the stellar rotational velocities of early-type stars, although the targets in the Small Magellanic Cloud may rotate faster than those in young Galactic clusters. The rotational velocity distribution for single non-supergiant B-type stars is inferred and implies that a significant number have low rotational velocity ($\approx 10\%$ with $v_e < 40 \text{ km s}^{-1}$), together with a peak in the probability distribution at $v_e \approx 300 \text{ km s}^{-1}$. Larger projected rotational velocity estimates have been found for our Be-type sample and imply that most have rotational velocities between 200–450 km s^{-1} .

Key words. stars: early-type – stars: atmospheres – stars: rotation – stars: evolution – Magellanic Clouds – open clusters and associations: individual: NGC 346

1. Introduction

Massive stars significantly influence the evolution of their host clusters and galaxies via feedback of both energy and chemically-processed material. To help reconcile evolutionary predictions of massive stars with observations, the effects of stellar rotation have been included in theoretical models (Heger & Langer 2000; Meynet & Maeder 2000) and applied to, for example, understanding the ratios of red-to-blue supergiants (Maeder & Meynet 2001) and the populations of Wolf–Rayet stars (Meynet & Maeder 2005; Vink & de Koter 2005).

One of the primary motivations for including rotation in massive-star models were observations of core-processed material, for example enhanced nitrogen abundances, on the stellar surface (see, e.g. Walborn 1970; Gies & Lambert 1992; Venn 1999; Bouret et al. 2003; Lennon et al. 2003; Korn et al. 2002, 2005). The process of rotational mixing then naturally explained how material could be mixed from the core to the surface. Additionally, rapid rotation may be a prerequisite in producing a

gamma-ray burst from a single massive star via its homogenous evolution (Yoon & Langer 2005; Woosley & Heger 2006).

A large observational sample of ~ 500 OB-type stars in the Galaxy and Magellanic Clouds was obtained by the FLAMES Survey of Massive Stars (hereafter FSMS, Evans et al. 2005, 2006) to investigate these topics. Surface nitrogen abundances estimated for the B-type samples in the FSMS (Hunter et al. 2007; Trundle et al. 2007; Hunter et al. 2008b,a) implied rotational mixing might not be the only transport mechanism involved, and the nature of these stars has been discussed further by, for example, Brott et al. (2011b), Maeder et al. (2014) and Aerts et al. (2014). O-type stars with low projected rotational velocities and abundances that appear inconsistent with rotational mixing were also identified by Rivero González et al. (2012).

In a second campaign, the VLT-FLAMES Tarantula Survey (Evans et al. 2011, hereafter VFVS), spectroscopy was obtained for ~ 800 targets in the 30 Doradus region of the Large Magellanic Cloud (LMC). Targets with enhanced surface nitrogen abundances, which appeared to be incompatible with current single-star models of rotational mixing, were again identified in both the O-type (Grin et al. 2017) and B-type (Dufton et al. 2018) populations. Definitive conclusions have been hampered

* Based on observations at the European Southern Observatory in programmes 171.D-0237 and 074D.0011

both by observational and theoretical uncertainties, and by the possibility of other evolutionary scenarios, such as binarity and magnetic fields (see Grin et al. 2017; Dufton et al. 2018, for further details). Nevertheless, rotation remains one of the critical parameters in the evolution of massive stars.

Theoretical models predict that massive stars at higher metallicity have stronger line-driven winds, thereby losing more mass and angular momentum over their lifetime compared to those at lower metallicities (Kudritzki et al. 1987; Kudritzki & Puls 2000; Vink & de Koter 2005; Mokiem et al. 2006). However, studies of rotational velocities of early-type stars from ultraviolet spectroscopy have found little compelling evidence for stars in the Clouds rotating more quickly than in the Galaxy (Penny et al. 2004; Penny & Gies 2009). Hunter et al. (2008b) presented rotational velocities for ~ 400 massive stars from optical spectroscopy in both the LMC and the Small Magellanic Cloud (SMC) and compared these with Galactic field stars to show that the predicted trend of rotational velocity and metallicity was observable. However, the analysis was complicated by the nature of the samples. Although the target stars in the Clouds were in the direction of young clusters, much of the sample was composed of field stars. Galactic studies have implied that stars in clusters rotate faster than those in the field (see, e.g. Strom et al. 2005; Dufton et al. 2006b; Huang & Gies 2006; Wolff et al. 2007), with a similar trend observed in the LMC (Keller 2004; Wolff et al. 2008). This would be consistent with the stars in the older field populations having spun down over their lifetimes. Alternatively, as suggested by Wolff et al. (2007), the star formation process may be affected by the properties of the ambient gas, with stars in clusters being born from more energetic material and having shorter lived magnetically-locked accretion discs.

Analysis of the VFTS data has yielded estimates of the rotational velocity distributions and atmospheric parameters for both the O-type (Ramírez-Agudelo et al. 2013, 2015; Grin et al. 2017) and B-type (Dufton et al. 2013, 2018; Garland et al. 2017) samples in the 30 Doradus region in the LMC. Here we present complementary observations of massive stars in the region of the cluster NGC 346 in the lower-metallicity environment of the SMC. Our observations can be combined with those for early-type stars previously observed towards this cluster by the FSMS. By using the same observational settings and tools as in the analysis of the FSMS and VFTS data we can minimise any systematic effects in the comparison of their fundamental parameters.

The observational material is presented in Sect. 2 and its spectral classification discussed in Sect. 3 and Appendix B. Sect. 4 describes the methods used to estimate the atmospheric parameters, projected rotational velocities, luminosity, masses and ages for our targets, which are then discussed in Sect. 5.

2. Observations

Spectroscopy was obtained using the Fibre Large Array Multi-Element Spectrograph (FLAMES, Pasquini et al. 2002) on the Very Large Telescope at the European Southern Observatory (ESO). The FLAMES–Medusa mode was used to feed light from typically 80 stellar targets (plus sky fibres) per fibre configuration to the Giraffe spectrograph. Our primary aim was to obtain a near-complete spectroscopic census of the O-type and early B-type populations of the NGC 346 region, with targets selected from the ESO Imaging Survey (EIS, Momany et al. 2001). Hereafter this spectroscopy will be designated the Survey dataset to distinguish it from the FSMS data.

A faint magnitude cut-off of $V \leq 16.75$ mag was employed to ensure that the signal-to-noise (S/N) ratios of the spectra were

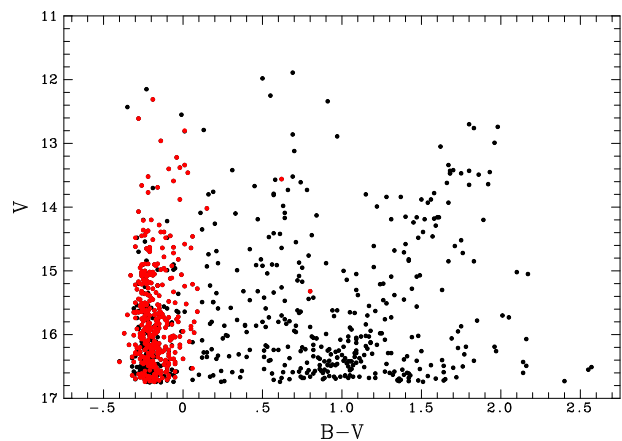


Fig. 1. Colour-magnitude diagram showing the location of the additional FLAMES targets combined with those from the FSMS (363 stars, red points) compared to all potential targets ($V \leq 16.75$) within a $10'$ search radius of the centre of the cluster.

sufficient for quantitative analysis. Adopting a distance modulus to the SMC of 18.9 (Harries et al. 2003; Hilditch et al. 2005), this corresponds to a latest (unreddened, main sequence) spectral type of approximately B3 V (cf. Walborn 1972). A colour cut of $(B - V) \leq 0.1$ was also employed to restrict the sample to OB-type stars, after allowing for a typical interstellar reddening for NGC 346 of $E(B - V) \sim 0.08$ (e.g. Hennekemper et al. 2008); similar criteria were previously employed in the selection of the FSMS targets. A colour-magnitude diagram for our targets and for the potential targets from the EIS catalogue (within a $10'$ search radius of the cluster centre) is shown in Fig. 1¹.

Astrometry and optical photometry for our targets are summarised in Table A.1. Identifications (sorted by V -band magnitude) have been assigned from #1001 to distinguish them from the FSMS targets; similar information for the latter is given in Table 4 of Evans et al. (2006). Also included in Table A.1 are radial distances of each target from #1001 (the brightest object in the central part of the cluster), following the approach in Table 1 of Hunter et al. (2008b).

The spatial distribution of our targets and those previously observed by the FSMS in the central region of NGC 346 are shown in Fig. 2. The FLAMES–Medusa fibres project to a diameter of $1''2$ on the sky, equivalent to 0.35 pc in the SMC, and therefore may include contributions from companions unresolved in the ground-based imaging. From inspection of *Hubble Space Telescope* (*HST*) images of NGC 346 (Sabbi et al. 2007), in all but one instance (#0111) our targets are by far the brightest source in the fibre aperture. This comparison was only possible for 82 of our 363 sources due to the limited extent of the *HST* imaging. However it includes the densest regions at the centre of the field (Fig. 2) where these effects might be expected to be most significant.

The radius of the ionised region of NGC 346 has been given as $3'5$ by Relaño et al. (2002) which, at the distance of the SMC, corresponds to a physical distance of 61 pc. Given the magnitude cut-off and colour selection, 125 stars from 167 potential targets were observed out to this radius, a completeness of 75%

¹Two ‘red’ stars were also observed. One is NGC 346-003 from the FSMS, observed with the fibre-feed to UVES (see Evans et al. 2006). The other (#1103) had spurious EIS photometry and was later supplemented by archival photometry (see Table A.1).

which rises to 88% for $V < 16.0$. The principal limitation on the completeness was the crowding of targets in the core of the cluster, and the minimum approach distance permitted for the Medusa fibre-heads. Nearly all of the bright stars in the central region without FLAMES spectroscopy have previous spectroscopy, leading for the first time to a comprehensive census of the high-mass spectroscopic content of NGC 346.

The observations were taken in service mode between 2004 September 27 and November 28. Three Medusa configurations with near-identical central positions (Fields ‘A’, ‘B’ and ‘C’) were observed as summarised in Table 1. Two of the standard Giraffe settings were used: LR02 (with a wavelength range of 3960 to 4564 Å at a spectral resolving power of $R \sim 7000$) and LR03 (4499–5071 Å, $R \sim 8500$). These gave full coverage of the blue optical region, with an overlap from $\lambda\lambda 4500$ –4565 Å. At least four exposures at each grating setting were taken for each field. In some cases the requirements on the observing conditions were not satisfied and observing blocks were repeated. As a consequence, six exposures were obtained at both settings for Field B, and eight for Field C. Although the time-sampling is not as extensive as that obtained in the FSMS, the observations offer some leverage on the detection of massive binaries.

As for the FSMS data², the Giraffe Base-line Reduction Software (girBLDRS; Blecha et al. 2003) was used for bias subtraction, flat-field correction, fibre extraction and wavelength calibration. The sky subtraction and correction to the heliocentric velocity frame was then undertaken using the STARLINK software DIPSO (Currie et al. 2014).

The multiple spectra of each target were first compared to search for evidence of radial-velocity variations – simple division of the spectra from one epoch into another can reveal ‘P Cygni’-like features for binary systems. The overlap region between the LR02 and LR03 settings helped in this regard as it contains useful stellar lines (e.g. He II $\lambda 4542$, Si III $\lambda 4552$) to increase the time cadence. Stars displaying radial-velocity variations significant enough to be detected from this simple approach ($\gtrsim 10 \text{ km s}^{-1}$) are considered as candidate single-lined binaries (SB1) in the final column of Table A.1. Similarly, targets clearly displaying multiple components are classified as double-lined binaries (SB2), and in one instance as a triple-lined binary (SB3).

For the apparently single stars, all usable spectra were combined either by simple addition or by using a median σ -clipping algorithm. The final spectra were normally indistinguishable apart from regions affected by cosmic rays where the latter method was superior. The full wavelength range for spectrum at each grating setting could usually be normalised using a single, low-order polynomial. However, for some features (e.g. the Balmer series), the combined spectra around individual (or groups of) lines were separately normalised.

Garland et al. (2017) have discussed the reduction of LR02 and LR03 FLAMES spectroscopy for targets which show significant radial-velocity variations. They found that even for narrow-lined stars (with $v_e \sin i \leq 40 \text{ km s}^{-1}$), simply combining exposures without velocity shifts led to no significant spectral degradation provided the range of radial velocities, Δv_r , was less than 30 km s^{-1} . For targets with larger projected rotational velocities, the maximum value of Δv_r increased, e.g. for $v_e \sin i \sim 120 \text{ km s}^{-1}$, it corresponded to $\Delta v_r \leq 100 \text{ km s}^{-1}$. Hence for the SB1 candidates, we have initially combined the exposures *without* any velocity shifts and estimated the $v_e \sin i$ as discussed in Sect. 4.2. We have then cross-correlated ex-

Table 1. Observing log of the FLAMES NGC 346 Survey observations.

Date	Field	Setting	λ_c [Å]	Exposure time [sec]
2004-09-27	A	LR02	4272	2×1725
2004-09-28	A	LR02	4272	2×1725
2004-10-01	A	LR03	4797	2×1725
2004-10-04	A	LR03	4797	2×1725
2004-10-14	B	LR02	4272	1×1725, 1×1234
2004-10-17	B	LR02	4272	2×1725
2004-10-18	B	LR03	4797	4×1725
2004-11-25	B	LR02	4272	2×1725
2004-11-25	B	LR03	4797	2×1725
2004-10-18	C	LR02	4272	4×1725
2004-10-18	C	LR03	4797	4×1725
2004-11-26	C	LR02	4272	4×1725
2004-11-26	C	LR03	4797	2×1725
2004-11-28	C	LR03	4797	2×1725

posures from individual epochs (see Table 1) to estimate Δv_r for each wavelength setting. The $v_e \sin i$ and Δv_r estimates for each wavelength setting in each target were then compared to the simulations of Garland et al. (2017). They were generally consistent with no significant spectral degradation, the only exceptions being: #1014 (LR02 and LR03 settings), #1023 (LR03), #1101 (LR02), #1182 (LR02), #1192 (LR03), #1196 (LR02), #1209 (LR03), #1241 (LR03), #1246 (LR03). The spectroscopy for these cases has been re-reduced with the individual exposures shifted in velocity space using the results from the cross-correlations. The projected rotational velocities were re-estimated, with the changes in the estimates always being less than 5%. For the ten additional Survey targets identified as SB2, the exposures for each epoch were combined separately.

3. Spectral classification

All the Survey spectroscopy has been classified with reference to criteria developed for massive stars in the low metallicity environment of the SMC (Lennon 1997; Walborn et al. 2000; Evans & Howarth 2003; Evans et al. 2004). Spectral classifications for all 247 targets are given in Table A.1³, together with previous published classifications. Cross-matches with past identifications were generally performed by visual comparison of published finding charts and the EIS images. In the case of the 2dF spectroscopy from Evans et al. (2004), stars were matched using their astrometric data and a conservative search radius of $1''$ (to avoid spurious matches). Previous classifications were principally from Massey et al. (1989, 19 stars), and Evans et al. (2004, 18 stars) and are included in the final column of Table A.1 in italics. Other classifications are included as footnotes to the table. Detailed comments on five targets of note are provided in Appendix B.

In general there was good agreement with previous classifications, although a few stars (e.g. #1048 and #1058) received later types than before, probably owing to the improved spectral resolution of the FLAMES data. While good nebular subtraction is difficult to achieve in fibre spectroscopy, He I nebular emission was typically resolved in the cores, highlighting the potential for infilling if degraded to lower resolution. We were also able to re-

²For the FSMS targets the normalised spectra were taken directly from the data archive available at: <https://star.pst.qub.ac.uk/~sjs/flames/>

³These were previously included in the compendium of SMC data by Bonanos et al. (2010) as ‘Hunter et al. in prep.’

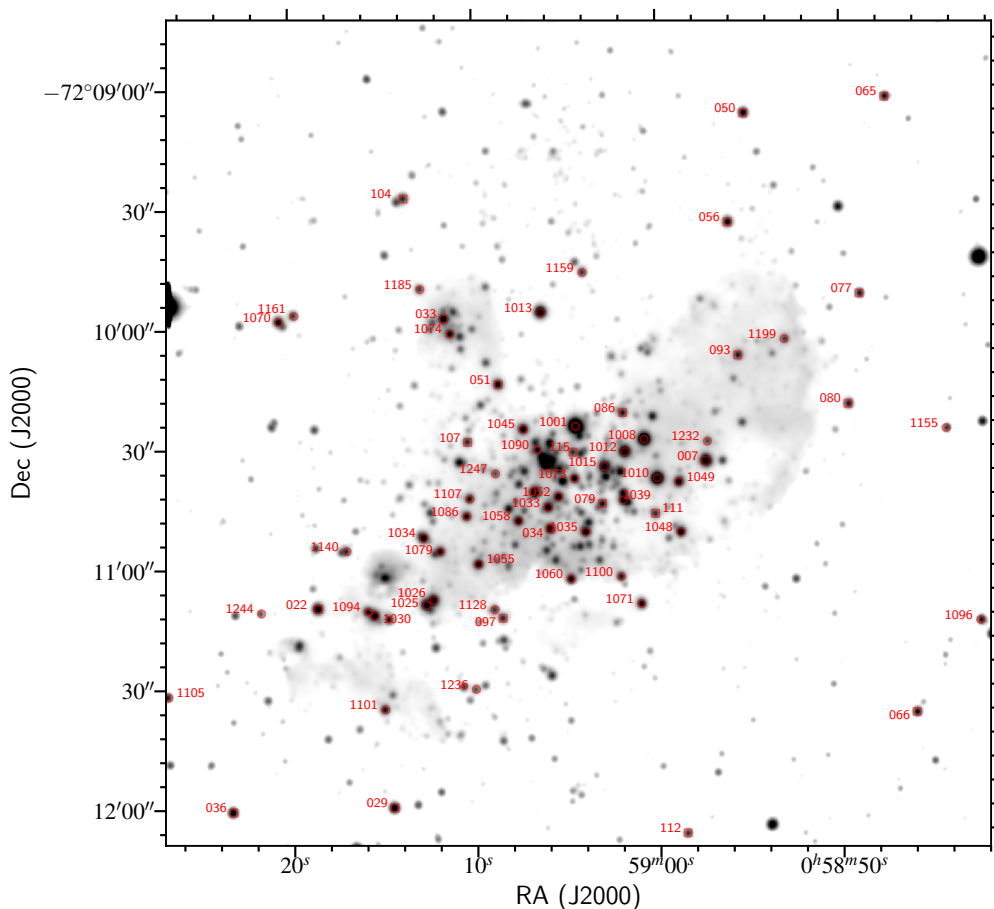


Fig. 2. FLAMES targets in the central $\sim 3/5$ of NGC 346. Targets with identifications >1000 are from the observations presented here, the remainder are from Evans et al. (2006).

fine some of the previously uncertain classifications from Evans et al. (2004).

The Survey data thus provide the first classifications for over 200 massive stars in this important region in the SMC, including ten new O-type stars (six of which are within $1/2$ of the centre). When combined with the FSMS spectroscopy from Evans et al. (2006), this represents a detailed spectral census of the NGC 346 cluster and its environs. A summary of the spectral content of the two observational samples is given in Table 2.

Twelve targets have been classified as O-type binaries (9 SB1, 2 SB2, 1 SB3) and fifty one as B-type binaries (36 SB1, 15 SB2). This translates into observed binary percentages (plus standard deviations assuming binomial statistics) of $26 \pm 6\%$ (O-type) and $18 \pm 2\%$ (B-type). For the VFTS survey of the Tarantula Nebula in the LMC, *observed* binary percentages of $35 \pm 3\%$ (O-type Sana et al. 2013) and $25 \pm 2\%$ (B-type Dunstall et al. 2015) were found. However, as discussed by those authors, the actual binary percentages will be larger due to some binaries not having been identified; from Monte-Carlo simulations they inferred *actual* binary percentages of more than 50% for both O- and B-type systems. Given the limited time cadence of our spec-

troscopy, our *observed* binary fractions appear consistent with those found from the VFTS.

Known omissions from our spectroscopy (due to crowding of the Medusa fibres) in the central part of the cluster include: MPG 395, 451, 468, and 487, with classifications from Massey et al. (1989) of B0 V, B0 V, O9 V, and O6.5 V, respectively; MPG 470, classified as O8-9 III:nw (Walborn & Blades 1986); the components of N66A, which include N66A-1 (O8 V, Heydari-Malayeri & Selier 2010); and MPG 375 ($V = 15.47$), for which the spectral type is unknown. With our focus on OB-type stars, we have also omitted HD 5980, the bright source on the eastern edge of Fig. 2, approx. 1.75 from the core of NGC 346. HD 5980 is a well-studied WR/LBV binary system, with some recent observations suggesting it is potentially a quadruple system (Koenigsberger et al. 2014).

4. Analysis

4.1. Atmospheric parameters

We have employed model-atmosphere grids calculated with the TLUSTY and SYNSPEC codes (Hubeny 1988; Hubeny & Lanz

Table 2. Spectral content of the NGC 346 region from the FSMS (Evans et al. 2006) and the Survey data. All of the Be-type spectra are of early B-type, except for two classified as B5 in the Survey dataset. #1024 has been classified as a Be-type star but see Appendix B for a detailed discussion of its spectrum.

Source	Total	O	Early-B [B0-3]	Be	Late-B [B5-9]	AFG
FSMS	116	19	59	25	2	11
Survey	247	28	149	45	8	17
Total	363	47	208	70	10	28

1995; Hubeny et al. 1998; Lanz & Hubeny 2007). They cover a range of effective temperature, $12\,000 \leq T_{\text{eff}} \leq 35\,000$ K in steps of typically 1500 K. Logarithmic gravities (in cm s^{-2}) range from 4.5 dex down to the Eddington limit in steps of 0.25 dex, and microturbulences are from 0–30 km s^{-1} in steps of 5 km s^{-1} . Grids have been calculated for a range of metallicities with that for an SMC metallicity used here. As discussed by Ryans et al. (2003) and Dufton et al. (2005), equivalent widths and line profiles interpolated within these grids are in good agreement with those calculated explicitly at the relevant atmospheric parameters. Full details of the grids can be found in Dufton et al. (2005).

The analysis followed similar methods to those used by Hunter et al. (2008b) when analysing the FSMS data and is only briefly summarised here. Where two (or more) ionisation stages of silicon were observed, the effective temperatures were constrained by requiring that each ionisation stage yielded the same estimated silicon abundance. For the B0 to B0.5 spectral types, the He II $\lambda 4542$ and $\lambda 4686$ lines were also observable and yielded estimates that were normally in good agreement with those from the silicon ionisation equilibrium. For spectral types later than B3, the strength of the He I spectrum becomes temperature sensitive and the well observed $\lambda 4026$ line was used.

Effective temperature estimates for the remaining stars have been taken from the effective temperature–spectral type calibration for the SMC of Trundle et al. (2007). We find that this calibration yields estimates that are in satisfactory agreement with those from the silicon and helium lines, with a mean difference of 460 ± 1220 K. Our sample contained targets with B2.5 V and B3 V types, which lie outside this calibration and for which we have no independent estimates from the silicon and helium lines. The effective temperature scales from Trundle et al. (2007) for the Galaxy and the SMC differ by typically 2500–3500 K and between the LMC and SMC by 500 K. We have therefore used these differences to estimate effective temperatures for the B2.5 V and B3 V types in the SMC. Finally, the effective temperature for two B2 II objects was taken as the mean of those for B2 I and B2 III. The adopted effective temperature calibration versus spectral type is summarised in Table 3.

In cases where we were unable to assign unique spectral types, we have assigned effective temperatures appropriate to the mid-points of the range. For spectra without luminosity classifications we have assumed that they are near main-sequence (class V) objects. As discussed in Section 4.3, the estimated luminosities are generally consistent with such a classification.

Surface gravities were determined by comparing rotationally-broadened theoretical profiles of the H δ and H γ lines to those observed. The surface gravity and effective temperature estimates are correlated and an iterative method was adopted to simultaneously determine these parameters. It should be noted that, as discussed by Dunstall et al. (2011),

surface gravity estimates for the Be-type stars may be too small due to continuum contamination from a circumstellar disc.

The analyses presented here have implicitly assumed that the targets are single, although a significant number of the apparently single targets may be the primary in a multiple system. Additionally we have estimated atmospheric parameters for 36 SB1 and 11 SB2 B-type systems. Garland et al. (2017) considered the consequences of an unseen secondary in their analysis of VFTS B-type binaries. Making the extreme assumption that the secondary had a featureless spectrum, they found that the estimated effective temperatures (from the silicon ionization equilibrium) and the gravities (from fitting hydrogen line profiles) were too small by typically 500–1000 K and 0.1–0.3 dex respectively. In reality, the situation will be more complicated as any secondary making a significant flux contribution is also likely to be a near main sequence B-type star but of slightly later spectral type than the primary. If its absorption features were incorporated into those of the primary (as is very likely for the broad hydrogen lines), the consequences could be different to those modelled by Garland et al. (2017). For example, as the hydrogen line spectrum in B-type stars strengthens as one moves to later spectral types, the gravity estimates could become *too large*. In summary, the atmospheric parameters for all the targets may contain additional uncertainties due to the presence of secondaries. However the discussion above implies that these are unlikely to be significantly larger than the stochastic uncertainties discussed below.

Twenty eight O-type stars were also observed, which are generally hotter than the models in our TLUSTY grid. Four have been analysed previously by Bouret et al. (2013) for #1008, #1012, and #1071⁴, and Heap et al. (2006) for #1019 and their estimates are listed in Table A.2. For the remainder we adopt temperatures using the calibration for O-type dwarfs from the analysis of ~ 30 O-type stars in the SMC by Mokiem et al. (2006, which included results for 21 of the stars observed in NGC 346 by the FSMS and is summarised in Table 3). Seven of the targets are designated as SB1 and the atmospheric parameters for these (and indeed) other O-type targets may be affected by the presence of unseen secondaries as discussed for the B-type sample. Given the complications of modelling the winds of O-type stars we do not attempt to derive surface gravities or wind parameters for these stars here.

The atmospheric parameters of our sample of stars are given in the Table A.2. For completeness, we also list the parameters from Hunter et al. (2008b) and Mokiem et al. (2006) for the FSMS sample⁵; when no atmospheric parameters were provided, we have followed the same spectral type methodology as for the Survey spectroscopy. Effective temperatures (and gravities) could not be estimated for 15 targets. Six were SB2 systems where the spectral type of the primary was uncertain, seven lay beyond our spectral type calibration (five B9 II and two B5e targets), and #1001 and #1024 had peculiar spectra (as discussed in Sects. B.1 and B.3, respectively). Additionally, no gravity estimate is given for #1038 (B0:e) as no convincing fit could be obtained for its Balmer line profiles.

Comparison of the effective temperatures derived from the silicon and helium lines for our sample and for B-type samples obtained with the same instrumentation in the LMC (Garland

⁴Estimates for #1008 and #1012 have also been presented by Bouret et al. (2003), Heap et al. (2006), and Massey et al. (2009).

⁵Hunter et al. (2008b) did not provide atmospheric parameters for #0111 although the He II spectrum is clearly present in the FSMS spectroscopy. We have therefore analysed this spectroscopy to obtain atmospheric parameters, although we note that the *HST* imaging reveals this to be a visual composite of two nearly equal magnitude sources.

Table 3. Adopted effective temperature–spectral type calibration.

Spectral type	Effective temperature		
	I	III	V
O5	–	–	45200 (M)
O6	–	–	42970 (M)
O7	–	–	40730 (M)
O8	–	–	38500 (M)
O9	–	–	36265 (M)
O9.5	–	–	35150 (M)
B0	27200 (T)	–	32000 (T)
B0.2	25750 (T)	–	30800 (T)
B0.5	24300 (T)	–	29650 (T)
B0.7	22850 (T)	25300 (T)	28450 (T)
B1	22350 (T)	23950 (T)	27300 (T)
B1.5	20650 (T)	22550 (T)	26100 (T)
B2	18950 (T)	21200 (T)	24950 (T)
B2.5	17200 (T)	19850 (T)	23900 (E)
B3	15500 (T)	18450 (T)	21500 (E)
B5	13800 (T)	–	–

Notes. The calibration for O-type dwarfs was assumed to be linear and was derived from fitting the results from Mokiem et al. (2006, M). The B-type values were primarily from Trundle et al. (2007, T) and extended by scaling from Galactic and LMC estimates from Trundle et al. (E).

et al. 2017; Dufton et al. 2018) imply that these estimates will have a stochastic uncertainty of typically $\pm 1\,000$ K. The effective temperature estimates deduced from the spectral type calibration will be more uncertain. The comparison with those estimated from the silicon and helium lines discussed above and the scatter in effective temperatures estimates for stars of the same spectral type implies that where the spectral type is well defined a conservative stochastic uncertainty of $\pm 1\,500$ K is appropriate. For those stars with a range of spectral types or no luminosity classification the uncertainties may be larger. For the surface gravity estimates, the values from the H δ and H γ lines generally agreed to within 0.1 dex. Taking into account the uncertainties in the effective temperature estimates, an error of 0.2 dex in the surface gravity would appear to be appropriate.

4.2. Projected rotational velocities

Projected rotational velocities have been estimated using two independent methodologies, viz. profile fitting (PF) and Fourier Transform (FT). For the former, the TLUSTY theoretical model at the closest grid point to the parameters given in Table A.2 was adopted. An absorption line profile was then scaled to have the same strength as that observed and the instrumental broadening was included by convolving with a Gaussian profile. The resulting profile was then rotationally broadened assuming a linear limb darkening law with $\epsilon=0.6$ (Gray 2005) until the best fit (by a χ^2 minimisation) with the observed profile was found. This method was used previously by Hunter et al. (2008b) where further details can be found.

Metal absorption lines, which are less affected by intrinsic broadening (than for example the hydrogen and diffuse helium lines) provide the most reliable estimates. For our B-type stars we have used either the Mg II $\lambda 4481$ or Si III $\lambda 4552$ lines, whichever was stronger. For stars with significant rotational ve-

locities the metal lines were not well defined, and we used the He I $\lambda 4026$ line. The rotational broadening of our targets was generally larger than the intrinsic broadening, so the choice of theoretical profile was not critical.

For the O-type stars we have adopted theoretical profiles from the grid of Lanz & Hubeny (2003). The mean surface gravity of the O-type dwarf stars from Mokiem et al. (2006) was $\log g \sim 4.15$ dex and we therefore adopted models from the closest effective temperature grid point with $\log g = 4.25$ dex. Our targets have spectral types later than O5 and hence the He I $\lambda 4026$ line was visible and was used to estimate projected rotational velocity, thereby maintaining consistency with analysis of the B-type stars. The PF estimates are listed in Table A.2 with those from the original FSMS data being taken directly from Hunter et al. (2009)⁶.

Independent estimates were obtained using the FT methodology (Carroll 1933; Simón-Díaz & Herrero 2007). This has been widely used for early-type stars (see, for example Dufton et al. 2006a; Lefever et al. 2007; Markova & Puls 2008; Simón-Díaz et al. 2010, 2017; Fraser et al. 2010; Dufton et al. 2013; Simón-Díaz & Herrero 2014) and relies on the convolution theorem (Gray 2005), viz. that the Fourier transform of convolved functions is proportional to the product of their individual Fourier Transforms. It then identifies the first minimum in the Fourier transform for a spectral line, which is assumed to be the first zero in the Fourier transform of the rotational broadening profile with the other broadening mechanisms exhibiting either no minima or only minima at higher frequencies. Further details on the implementation of this methodology are given by Simón-Díaz & Herrero (2007) and Dufton et al. (2013). Estimates were obtained for the targets observed here and those in the FSMS and are listed in Table A.2. For the SB2 systems the estimates refer to the primary, which is defined as the star having the strongest absorption spectrum. Values were only measured for SB2 systems where the two spectra were well separated in at least one epoch.

The moderate spectral resolving power of our LR02 and LR03 spectra corresponds to a velocity resolution of approximately 40 km s^{-1} . This made the estimation of the projected rotational velocities in the sharpest lined stars unreliable. For the PF methodology, the instrumental broadening dominated the observed profiles, while estimates also became more sensitive to the intrinsic profile adopted. For the FT methodology, the position of the first minima (at relatively high frequencies in the Fourier Transform) became difficult to identify. Hence when projected rotational velocity estimates were less than 40 km s^{-1} , they have been assigned to a bin with $0 \leq v_e \sin i \leq 40 \text{ km s}^{-1}$. For consistency the same approach has been adopted for the previously published PF estimates for the FSMS data. Sixty one targets fell into this category, with 54 targets having estimates of $\leq 40 \text{ km s}^{-1}$ using both methodologies. One target had no FT estimate, while for the remaining six objects the larger (three PF and three FT) estimates ranged from $43\text{--}51 \text{ km s}^{-1}$ implying that they were consistent within the uncertainties discussed below.

For the 47 O-type stars, PF estimates could be obtained for all targets, apart from #1010, which has been classified as SB3 with asymmetric profiles; additionally, no convincing minimum was found for #1030 using the FT methodology. Estimates with $v_e \sin i \geq 40 \text{ km s}^{-1}$ were obtained for 36 targets and yielded a mean difference (FT-PF) of $4 \pm 16 \text{ km s}^{-1}$ and a mean ratio (FT/PF) of 1.04 ± 0.11 .

⁶For nine FSMS targets, where no values were tabulated, PF estimates have been obtained as discussed above.

For the larger B-type sample of 288 targets, 275 PF estimates were available. For those without measurement: five targets were classified as B9 II and lay beyond the low effective temperature limit of our grid, seven targets were classified as SB2, while no convincing fit could be found for #1024 (see Sect. B.3). For the FT methodology, 274 estimates were obtained; again no estimates were obtained for the SB2, B9 II targets and #1024, while no convincing minima could be found in the SB2 target, #0035. Estimates with $v_e \sin i \geq 40 \text{ km s}^{-1}$ for both methodologies were obtained for 223 B-type targets and yielded a mean difference of $1 \pm 12 \text{ km s}^{-1}$ and a mean ratio of 1.01 ± 0.09 . The statistics for the FSMS (61 targets, $-1 \pm 11 \text{ km s}^{-1}$, 0.99 ± 0.07) and Survey (162 targets, $2 \pm 13 \text{ km s}^{-1}$, 1.02 ± 0.09) were similar.

These statistics imply that the estimates from the two methodologies are in good agreement. The larger errors for the O-type sample may be due to the intrinsic weakness of the He I spectra and/or the larger macroturbulences that have been inferred for these spectral types (Simón-Díaz & Herrero 2014; Simón-Díaz et al. 2017). We have adopted conservative stochastic uncertainties of $\sim 10\%$ for the larger estimates and $\pm 10 \text{ km s}^{-1}$ for the estimates with $v_e \sin i < 100 \text{ km s}^{-1}$.

4.3. Luminosities

Luminosities have been calculated using the methodology described by Hunter et al. (2007). A uniform reddening of $E(B - V) = 0.09$ (Massey et al. 1995) with a reddening law of $A_V = 2.72E(B - V)$ (Bouchet et al. 1985) and a distance modulus of 18.91 dex (Hilditch et al. 2005) were adopted. Bolometric corrections from Vacca et al. (1996) and Balona (1994) were used for stars hotter and cooler than 28 000 K, respectively. Luminosity estimates were estimated for all targets apart from the 15 stars without effective temperature estimates (see Sect. 4.1) and are listed in Table A.2. The main sources of uncertainty will arise from the bolometric correction and the extinction. We estimate that these will typically contribute a stochastic error of ± 0.5 in the absolute magnitude corresponding to ± 0.2 dex in the luminosity. For stars in the innermost part of the cluster the adopted PSF-fitting photometry might have been influenced by the diffuse light from unresolved fainter stars. This is generally less than 10% compared to the magnitudes of our sources and less significant than the uncertainties already discussed. Additionally, there may be a systematic error due to the adopted distance to the SMC. Hilditch et al. (2005) estimated an uncertainty in their distance modulus of ~ 0.1 , which would translate to a systematic error in the luminosity estimates of 0.04 dex.

As discussed in Sect. 4.1, for the 66 targets with no luminosity class, an effective temperature appropriate to a luminosity class V was adopted. Most of these have estimated luminosities consistent with them being close to the main sequence. However 13 targets have luminosities that are more than 0.3 dex larger than this main sequence luminosity (identified by a linear fit between luminosity and effective temperature for all targets with a luminosity class V designation). Hence the use of a luminosity class V calibration to estimate the effective temperature may not be appropriate; we have identified these targets in Table A.2 and their physical parameters should be treated with caution.

4.4. Masses and ages

We have used BONNSAI⁷ to estimate the evolutionary masses and ages of the stars in our samples. BONNSAI uses a Bayesian methodology and the grids of models from Brott et al. (2011a) to constrain the evolutionary status of a given star, including its age and mass (see Schneider et al. 2014, for details). As independent prior functions, we adopted the SMC metallicity grid of models, a Salpeter (1955) initial mass function, the initial rotational velocity distribution estimated by Hunter et al. (2008b), a random orientation of spin axes, and a uniform age distribution. The estimates of effective temperature, luminosity and FT projected rotational velocity (taken from Table A.2) were then used to constrain masses. For all targets, the predicted current and initial masses were very similar with differences $< 5\%$ and in Table A.2, we have therefore only listed the current mass estimates.

Using the adopted errors on the effective temperature (see Sect. 4.1), luminosity (Sect. 4.3) and projected rotational velocities (Sect. 4.2), BONNSAI returned 1σ -uncertainties for all the quantities that it estimates. In the case of the stellar masses, these were generally 6-8% and never greater than 10%. For the ages, the errors were normally 10-15% (and always less than 20%) for targets with estimated ages greater than 5 Myr. For younger targets the absolute error in the age estimates was typically 1-2 Myr. The corresponding larger fractional uncertainty reflects the position of the targets close to the zero age main sequence (ZAMS) and indeed for the youngest targets the lower error bound was consistent with the target lying on the ZAMS.

There may be additional uncertainties due to binarity or line-of-sight composites (unresolved at the distance of the SMC). These could affect the effective temperature estimates as discussed in Sect. 4.1 and also lead to an overestimate of the luminosity for the primary. We have investigated the consequences of this by *arbitrarily* decreasing the luminosity estimates for #0043 (B0 V) and #0099 (B2 III) by 0.2 dex (corresponding to a secondary flux contribution of approximately 35%); these apparently single stars were chosen as their effective temperature estimates lie at the upper and lower ranges of our B-type sample. Mass estimates were reduced by $\sim 10\%$ for both stars with the age estimates decreasing by 10% and increasing by 15% respectively. Hence even for apparently single stars care must be taken when interpreting these estimates.

For the SB2 target, #0013, BONNSAI mass estimates can be compared with those deduced from the orbital analysis by Ritchie et al. (2012). The BONNSAI estimate in Table A.1 is based on an uncertain spectral type (B1:) for the brighter component and a luminosity estimate that has not been corrected for binarity. As such it is larger than that found for the brighter component by Ritchie et al. (2012, $11.9 \pm 0.6 M_{\odot}$). We can also compare mass estimates based on the stellar parameters given by Ritchie et al. (2012) and our estimated system luminosity. For the brighter component, this leads to an effective temperature of $24\,500 \pm 1\,500$, $\log L/L_{\odot}$ of 4.67 ± 0.2 dex and $v_e \sin i$ of $110 \pm 10 \text{ km s}^{-1}$; the values for the secondary component are $34\,500 \pm 3\,000$ K, 4.50 ± 0.2 dex and $320 \pm 30 \text{ km s}^{-1}$ respectively. BONNSAI returns mass estimates of $12.8^{+1.9}_{-1.7}$ and $16.0^{+2.4}_{-2.1} M_{\odot}$, compared with 11.9 ± 0.6 and $19.1 \pm 1.0 M_{\odot}$ from Ritchie et al. (2012). Within the error bars, the estimates are in reasonable agreement, and indeed decreasing the adopted luminosity ratio would improve the agreement for both components.

⁷The BONNSAI web-service is available at: www.astro.uni-bonn.de/stars/bonnsai.

This is consistent with the good agreement that Schneider et al. (2014) found in their BONNSAI analysis of Galactic binaries.

Estimates could not be obtained for 22 targets. Fifteen had no effective temperature estimates (see Sect. 4.1) and hence no luminosity estimates as their bolometric corrections were unknown. As such they had insufficient constraints to estimate masses or ages. The remaining seven targets failed the posterior predictive check and/or a χ^2 -test. These were all classified as supergiants - four B8Ib/II, and three B1.5-B3 spectral types. For the former it was also not possible to find solutions using the effective temperature, gravity and $v_e \sin i$ estimates as constraints, implying that the models of Brott et al. (2011a) did not cover these stellar parameters. For the three remaining targets, solutions could be found using these constraints but implied logarithmic luminosities (in solar units) of 5.83-5.95 dex. These are far higher than those found in Sect. 4.3 and may be related to a mass discrepancy discussed by, for example, Herrero et al. (1992) and Markova et al. (2018). Hence we have not included these mass and age estimates in Table A.2.

In Sect.4.2, projected rotational velocities were estimated for our sample and in Sect.5.3.6, these are deconvolved to estimate the rotational velocity distribution. This is similar to that estimated by Hunter et al. (2008b) but shows evidence for a double peaked structure. Previously Schneider et al. (2017, Appendix A) found that the different choices of the rotational velocity distribution could lead to significant differences in the mass and age estimates.

Hence in order to investigate the sensitivity of our estimates to the adopted distribution, we have considered two alternatives – a flat distribution (with any rotational velocity being equally probable) and that found for B-type stars in 30 Doradus, which shows similar evidence for a double peaked structure (see Fig. 7). Targets with projected rotational velocities of approximately 100, 200 and 300 km s^{-1} and effective temperatures of approximately 20 000 and 30 000 K were analysed with the results summarized in Table 4. In general, different rotational velocity distributions lead to very similar estimates of the stellar mass and luminosity. Indeed in over half the cases, there is no change in the estimates as BONNSAI selected the same evolutionary models. The maximum ranges in mass and age estimates are only 0.2 M_\odot and 0.5 Myr respectively. As these are both lower than the uncertainties in the estimates discussed above, we conclude that uncertainties due to the choice of rotational velocity distribution are unlikely to be significant at least for targets near the hydrogen burning main sequence.

5. Discussion

We now discuss our estimates of the stellar parameters and projected rotational velocities obtained in Sect. 4. We generally adopt our FT estimates of the latter but also consider the PF estimates when they might lead to different conclusions.

5.1. Stellar masses and ages

As discussed by Indu & Subramaniam (2011), the SMC has experienced significant recent star formation with peaks at 0-10 Myr and 50-60 Myr. Unlike the LMC, where this activity has been concentrated in the north and north-eastern regions, recent star formation in the SMC has not been found to have significant spatial structure. NGC 346 as a young association is located in the central part of the brightest SMC H II region, N66 (Henize 1956); its structure has been discussed by, for example, Gouliermis et al. (2008) and Hennekemper et al. (2008).

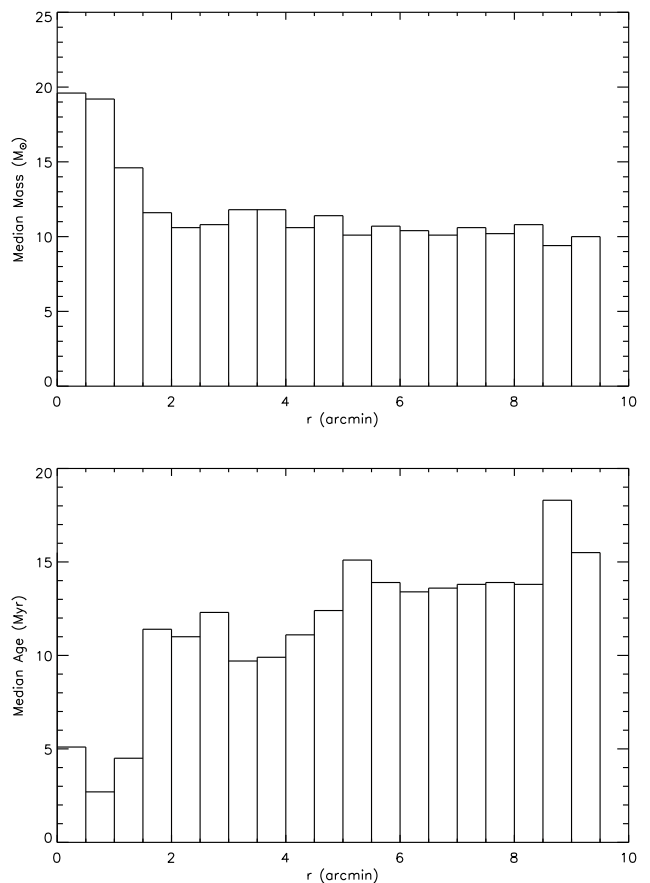


Fig. 3. Median stellar mass (top) and age (bottom) distributions for our NGC 346 spectroscopic sample as a function of radial distance from #1001.

Deep imaging from the *HST* has been used by Sabbi et al. (2008) to investigate the spatial variation of the present day mass function in the central part of NGC 346 (with an outer radius of approximately 20 pc, equivalent to $\sim 1'.13$). They found a steeper mass function with increasing radius, implying mass segregation for the most massive stars. The medians of the estimated stellar masses and ages (see Table A.2) for our spectroscopic sample are shown as a function of radius (r) from the centre of NGC 346 in Fig. 3. Our adopted centre was $12''$ from that determined by Sabbi et al., from a consideration of source counts but this will not impact significantly on the discussion below.

Stars with radial distances, $r \lesssim 2.0$, appear to be more massive, with a relatively flat distribution at larger distances. Additionally, these targets have smaller evolutionary age estimates. Kolmogorov-Smirnov (K-S) tests (Fasano & Franceschini 1987) for both the estimated masses and ages return very low ($<0.1\%$) probabilities that the samples from the inner and outer regions originated from the same parent population. Indeed, the mass distribution suggests that the stars are not bound to the central cluster, in agreement with the definition of NGC 346 by Gieles & Portegies Zwart (2011) as an ‘association’, and reflecting the arguments by Gouliermis et al. (2014) that it is comprised of two distinct components (with an extended distribution of stars that formed hierarchically in addition to the centrally-condensed cluster).

This decrease in the stellar mass and increase in the age estimates with radial distance mirrors the results of Sabbi et al.

Table 4. Estimates of the mass (in units of M_{\odot}) and age (in Myr) for different choices of the rotational velocity distribution. Estimates are provided for the adopted distribution of Hunter et al. (2008b) (H08), a flat distribution (Flat) and the distribution found by Dufton et al. (2013) for B-type stars in 30 Doradus (30 Dor) and are given to one decimal place to aid comparisons. Other stellar parameters are taken from Table A.2.

Star	T_{eff}	$\log L$	$v_e \sin i$	H08		Flat		VFTS	
				Mass	Age	Mass	Age	Mass	Age
0099	18 000	3.79	98	7.0	36.8	7.0	36.8	7.0	36.8
0070	30 500	4.43	102	13.8	7.9	13.8	7.8	13.8	7.7
1088	19 850	4.06	184	8.6	24.7	8.8	24.7	8.6	24.7
1230	29 650	4.06	198	11.8	3.9	11.8	3.4	11.8	3.5
1212	21 500	3.78	307	8.0	24.0	8.0	24.0	8.0	24.0
0079	29 500	4.37	308	13.4	8.0	13.4	7.8	13.4	7.9

(2008) for the inner region of NGC 346. It is also consistent with previous studies of the young stellar populations in our Galaxy and the LMC. For the former, Getman et al. (2014b,a) identified similar trends for pre-main sequence (PMS) stars in the Orion molecular cloud complex, whilst recently Getman et al. (2018) found that 80% of a sample of 19 young clusters exhibited radial age gradients. For the latter, Schneider et al. (2018) deduced ages and masses for approximately 450 apparently single early-type stars in 30 Doradus observed by the VFTS. The medians for the ages and masses as a function of increasing distance from the central R136 star cluster show an increase and decrease respectively, in agreement with our results and those for the Galactic studies. Hence there is increasing evidence that such behaviour may be an ubiquitous feature of massive star formation.

Adopting the threshold of $r < 2/0$ implied by Fig. 3 (rather than the $r \simeq 3/5$ from Relaño et al. 2002), Hertzsprung–Russell (H–R) diagrams for the inner and outer regions are shown in Fig. 4. Evolutionary tracks and isochrones are from the SMC grid of Brott et al. (2011a) with initial rotational velocities of 180 km s^{-1} , which is consistent with the median NGC 346 projected rotational velocity of 136 km s^{-1} and a random inclination of axes. However for targets near to the main sequence, the evolutionary tracks and isochrones are relatively insensitive to the choice of initial rotational velocity as can be seen from Figs. 5 and 7 of Brott et al. (2011a). Our choice of model grid maintains consistency with the masses and ages estimated using BONNSAI. SMC evolutionary models generated with the Geneva evolutionary code (Georgy et al. 2013a) have qualitatively similar tracks and isochrones but are only available for two initial rotational velocities. Hence we have not tried to use them to estimate masses and ages, although Dufton et al. (2018) found that for VFTS targets with low $v_e \sin i$, the Geneva tracks with zero rotation (Georgy et al. 2013b) yielded masses and ages that were consistent with the BONNSAI estimates within the observational uncertainties.

A significant number of targets lie above the ZAMS and imply a range of stellar ages (cf. the isochrones in Fig. 4) as discussed in Sect. 4.4. Nonetheless, there may be other causes, for example some of these may be either detected (SB1 or SB2) or undetected binaries with the luminosity of the primary being overestimated. For a binary containing targets with a flux ratio of unity, this overestimate would be 0.3 dex, which would constitute an upper bound. Inspection of Fig. 4 shows that particularly in the outer region a decrease of even 0.3 dex in the luminosity would not bring most of the targets to the ZAMS. Previous investigations of young Galactic clusters (see, for example, Strom et al. 2005; Dufton et al. 2006b) have also found targets above

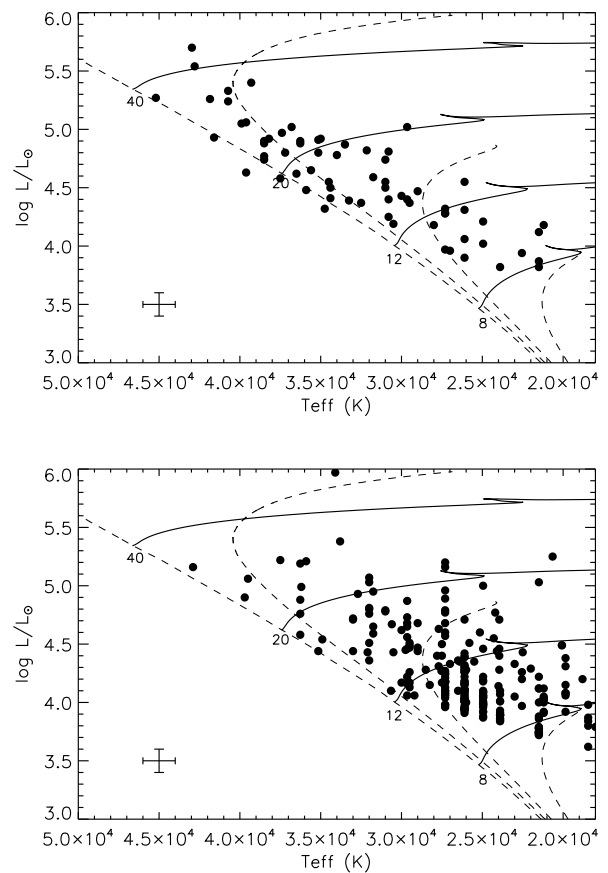


Fig. 4. Hertzsprung–Russell diagrams of the inner ($r < 2/0$, upper panel) and outer ($r > 2/0$, lower panel) regions from our combined NGC 346 sample. Evolutionary tracks are for an initial rotational velocity of approximately 180 km s^{-1} . Isochrones (dotted lines) are for, from left-to-right: 0, 3, 10 and 30 Myr.

the main sequence, despite a better discrimination against binarity. Additionally it is possible that some of the targets may be pre-main sequence. However in that case it would be expected that more overluminous stars would be present in the inner region, whilst if anything the reverse would appear to be the case.

Thirteen targets (twelve classified as O-type and one as B0V) have BONNSAI age estimates of less than 1 Myr and $1-\sigma$ upper

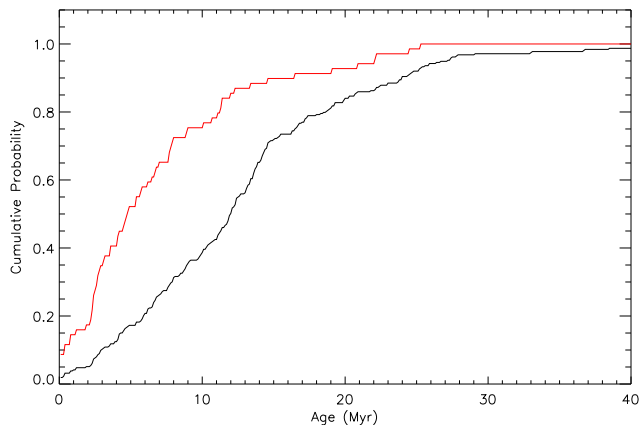


Fig. 5. Cumulative probability function for all 313 targets in NGC 346 with age estimates (solid black line) and for the 69 targets with radial distances of less than $2'$ (red line).

uncertainties ranging from 0.6 to 2.3 Myr. Combining these age estimates and uncertainties to find $1-\sigma$ upper limits on the ages leads to a range of 1.0-2.6 Myr with a median of 1.9 Myr. Hence these massive stars (mainly situated in the inner region) argue for an age of less than 2 Myr for the more recent period of star formation (in agreement with the estimate from Walborn et al. 2000, based on four stars close to the zero-age main sequence).

However it would appear that even the inner region of NGC 346 is not a simple, coeval stellar population – consistent with VFTS investigations of 30 Doradus (Schneider et al. 2018). Stars in this region (upper panel of Fig. 4) straddle several isochrones and it is clear that the cluster is more complex than just a simple single population (e.g. Cignoni et al. 2011; Gouliermis et al. 2014).

Inspection of the targets with the largest age estimates (30-42 Myr) shows that they are all classified as B3 III. The corresponding dwarf B3 V population, which would be expected to be younger, lies near the magnitude of the observational cutoff (see Sect. 2) and may not have been well sampled. However Fig. 3 confirms that stars in the outer region of NGC 346 generally appear older. Note that the intermediate-age cluster BS 90 (Bica & Schmitt 1995) is only a couple of arcminutes to the north of NGC 346, but is sufficiently old (4.5 Gyr, Sabbi et al. 2007; Rochau et al. 2007) that it does not contaminate our spectroscopic sample.

In Fig. 5, the cumulative probability distribution (CPD) is shown for all the NGC 346 age estimates. It is consistent with multiple generations or, effectively, continuous star formation, as discussed by Brott et al. (2011b) for the FLAMES fields observed in the LMC. A histogram of the age distribution shows significant star formation for the last 28 Myr peaking at an age of approximately 16 Myr. As discussed above, our sample will be a mixture of cluster members and field stars. We have therefore repeated the above procedures for the 69 targets within a $2'$ radius of our adopted centre of NGC 346. As can be seen in Fig. 5, these targets are (as expected) younger and imply significant star formation in the last 12 Myr peaking in the last 4 Myr. As this sample may also contain older field stars, this points to NGC 346 being dominated by a very young stellar population.

Table 5. Proper motions (mas yr^{-1}) and radial distances (r) from the centre of NGC 346 for selected targets from the DR2 *Gaia* data release. Also listed are the median values for targets with $r < 10'$ from the centre of NGC 346 and with $G \leq 16$ mag.

Target	ST	r		Proper motions (<i>Gaia</i>)	
		[']	[pc]	μ_{RA}	μ_{Dec}
0046	O7 Vn	3.8	66.9	0.80 ± 0.08	-1.22 ± 0.06
1114	O9 V	6.2	109.2	1.05 ± 0.10	-1.22 ± 0.07
1144	O9.5 V	4.0	70.4	1.01 ± 0.14	-1.25 ± 0.08
1134	B0:e	2.5	44.0	0.82 ± 0.09	-1.34 ± 0.06
1174	B1-3e	6.5	114.5	0.97 ± 0.10	-1.25 ± 0.08
Median	–	< 10.0	< 176.1	0.80	-1.22

5.2. O-type stars outside the central cluster

Three of the young O-type targets (#0046, #1114 and #1144) lie outside the inner region at radial distances between $3.8'$ and $6.2'$. We have used the *Gaia* DR2 data release (Gaia Collaboration et al. 2016, 2018) to search for peculiarities in their proper motions (see Table 5) consistent with them having been formed in the inner region. For a $10'$ radius centred on NGC 346, there are approximately 1700 targets with $G \leq 16$ and with proper motion estimates. These will be a combination of foreground and SMC targets but inspection of the proper motion distributions imply that they are heavily weighted to the latter. The median values of this sample are $\mu_{\text{RA}} = 0.80 \text{ mas yr}^{-1}$ and $\mu_{\text{Dec}} = -1.22 \text{ mas yr}^{-1}$.

In only one case (the μ_{RA} of #1114) is there a difference from the median value that is significant at a 2σ -level. This star also has the largest radial distance of the three, lying to the south east of the centre at a separation of $\delta_{\text{RA}} = 5.67$ and $\delta_{\text{Dec}} = 2.52$. Assuming it was ejected from the centre of NGC 346 soon after birth, its estimated age of 0.4 Myr would lead to a peculiar proper motion of 0.85 mas yr^{-1} . This is substantially larger than its proper motion relative to NGC 346, i.e. $\delta(\mu_{\text{RA}}) = 0.25 \text{ mas yr}^{-1}$. However, the age of this object is relatively poorly constrained with a $1-\sigma$ upper uncertainty of 1.9 Myr. Increasing the age to 2.3 Myr would then reduce the required $\delta(\mu_{\text{RA}})$ to 0.15 mas yr^{-1} , consistent with the *Gaia* values. The separation in declination implies $\delta(\mu_{\text{Dec}})$ of -0.38 and $-0.07 \text{ mas yr}^{-1}$ for the two ages, the latter being consistent with the effectively zero $\delta(\mu_{\text{Dec}})$ implied by the *Gaia* estimates.

For #0046, the *Gaia* estimates imply effectively zero proper motion with respect to NGC 346. The estimated age (1.0 Myr) and upper uncertainty (0.9 Myr) lead to predicted (relative) proper motions as small as $\delta(\mu_{\text{RA}}) = 0.07 \text{ mas yr}^{-1}$ and $\delta(\mu_{\text{Dec}}) = -0.10 \text{ mas yr}^{-1}$. These are consistent with the *Gaia* estimates within the observational uncertainties, particularly when considering the simple method used to ascertain the motion of NGC 346. Similar arguments apply to the proper motion estimates for #1144. In summary, the proper motions and age estimates for all three stars are consistent with them having been formed close to the centre of NGC 346, although the uncertainties do not preclude them having been formed elsewhere.

5.3. Stellar rotational velocities

5.3.1. General properties

Projected rotational estimates have been obtained for effectively all our targets classified earlier than B9 with only seven SB2 systems, the one SB3 system and the peculiar target #1024 (see

Sect. B.3) having no estimates. The sample is predominantly B-type with 275 estimates compared with 46 O-type values. Additionally there are 21 OB-type supergiants (luminosity classes I-II) with 16 $v_e \sin i$ estimates. Significant macroturbulence has been found previously in O-type and early B-type supergiants (Ryans et al. 2002; Simón-Díaz & Herrero 2014; Simón-Díaz et al. 2017). This would lead to our PF estimates (that include all excess broadening) being larger than the FT estimates (only the rotational component) and indeed a difference of $11 \pm 9 \text{ km s}^{-1}$ is found.

The estimates cover a wide range of projected rotational velocities from less than 40 km s^{-1} to approximately 380 km s^{-1} . Dividing the sample into 40 km s^{-1} bins, the most populous is that with $0 < v_e \sin i \leq 40 \text{ km s}^{-1}$, which implies that the sample contains a significant number of slowly rotating stars. This is confirmed by the deconvolution of the projected rotational velocity distribution discussed in Sect. 5.3.6. Additionally there are two very rapidly rotating targets, #1134 and #1174, which are discussed further in Sect. 5.3.4.

5.3.2. Mass variations

Hunter et al. (2008a) found lower projected rotational velocities for apparently single stars in the FSMS sample with $M > 25 M_\odot$ compared to those with lower masses in both the Magellanic Clouds and our Galaxy. This was true even in the low metallicity SMC, where the effects of line-driven winds are expected to be weaker (Mokiem et al. 2007), although their high-mass sample was limited to only six stars.

Our sample of non-supergiant targets that have mass estimates $M \geq 25 M_\odot$ is over a factor of two larger with 14 objects. Again these targets have a lower median⁸ FT $v_e \sin i$ estimate of 72 km s^{-1} compared with 137 km s^{-1} for the remaining targets; for the PF estimates the medians are 61 and 144 km s^{-1} respectively. K–S tests (setting all the upper limits of the $v_e \sin i$ estimates to 40 km s^{-1}) returned probabilities of 8.4% (PF estimates) and 12.3%, implying that differences in the projected rotational velocities of the two samples do not have a high level of statistical significance.

Projected rotational velocities have also been determined for both the O-type (Ramírez-Agudelo et al. 2013, 2015) and B-type (Dufton et al. 2013; Garland et al. 2017) stars in the VFTS of 30 Doradus; unfortunately mass estimates are not available for all the targets. However the LMC models of Brott et al. (2011a) imply that $25 M_\odot$ models should have a ZAMS effective temperature of 38000–39500 K, depending on the rotational velocity. In turn, the analysis by Ramírez-Agudelo et al. (2017) of the VFTS spectroscopy implies that this should correspond to a spectral type of O6.5 for luminosity class III–V objects. Hence we have repeated the above analysis for the apparently single non-supergiant VFTS targets and find median $v_e \sin i$ estimates of 111 km s^{-1} for the 55 early-O type targets cf. 173 km s^{-1} for the remaining 406 lower-mass objects. Although these are higher than the medians for the NGC 346 targets, they show the same qualitative behaviour. Additionally a K–S test returns a very low ($< 0.1\%$) probability that the projected rotational velocities for two 30 Doradus samples originated from the same parent population.

Further evidence for such a difference is provided by the estimated *rotational velocity* distributions for the apparently single non-supergiant VFTS O-type (Ramírez-Agudelo et al. 2013)

⁸It was not possible to calculate means given the significant number of targets with $v_e \sin i \lesssim 40 \text{ km s}^{-1}$.

Table 6. Medians of $v_e \sin i$ estimates of single non-supergiant B-type stars for the inner and outer regions of NGC 346 obtained by the profile fitting (PF) and Fourier transform (FT) methods, together with the number of stars in each sample (N).

Region	N	Medians	
		PF	FT
NGC 346 ($r < 2'0$)	33	187	195
NGC 346 ($r > 2'0$)	187	143	137
NGC 330	72	143	–
30 Doradus	250	–	195
NGC 6611	24	134	–

Notes. Results for NGC 330 and 30 Doradus are median values for the ‘field-like’ samples from Hunter et al. (2008b) and Dufton et al. (2013), respectively. Results for the Galactic cluster NGC 6611 are from Dufton et al. (2006b).

and B-type (Dufton et al. 2013) samples. The former appears unimodal with a mode at approximately 100 km s^{-1} and an extended higher velocity tail, while the latter is bi-modal with maxima at 60 and 300 km s^{-1} . In turn this leads to median rotational velocities of 160 km s^{-1} and 250 km s^{-1} , respectively. The LMC models of Brott et al. (2011a) imply that the boundary between the two samples will be at a mass of $16 M_\odot$. Although this boundary differs from that considered above of $25 M_\odot$, the medians again indicate that the more massive stars in general have lower rotational velocities.

In summary there is evidence that in the LMC, targets with masses, $M \geq 25 M_\odot$, have lower median projected rotational velocities than less massive early-type stars. A similar difference is seen in our results for the smaller sample in NGC 346, but it is not as statistically significant.

5.3.3. Spatial variations

B-type stars in Galactic clusters (see, for example Huang & Gies 2006; Wolff et al. 2007) appear to rotate more quickly than those in the field, with some evidence in support of this in the LMC (Keller 2004). In Sect. 5.1, targets within $2'0$ of the cluster centre were found to have a higher median mass and a smaller median age than the rest of the sample. We have therefore calculated medians for the $v_e \sin i$ estimates of the apparently single B-type stars (excluding luminosity class I–II supergiants) in these two spatial regions and summarize the results in Table 6.⁸

In Table 6, we also list the medians from the FSMS $v_e \sin i$ estimates of Hunter et al. (2008b) toward the SMC cluster, NGC 330 (adopting the same selection criteria as for NGC 346). These were obtained using a PF methodology similar to that adopted here and provide a predominantly SMC ‘field-like’ sample as the large majority lie well beyond the cluster radius (see Evans et al. 2006). We find that the median projected rotational velocities in the outer region of NGC 346 and in the (predominantly field sample) of NGC 330 are in good agreement. Although both samples are almost certainly not purely field stars (and NGC 330 is older than NGC 346), these results serve to illustrate the slower rotational velocities compared to the inner region of NGC 346 in agreement with the Galactic studies.

The stars at larger radial distances have on average larger ages than those within the inner $2'0$ of the cluster as discussed in Sect. 5.1. Hence the variation in median projected rotational velocity may reflect the stellar rotation decreasing as the stars evolve during their hydrogen core burning phase. Inspection of the SMC models of B-type stars by Brott et al. (2011a) shows

that this can occur with rotational velocities decreasing by up to 20%. However this is limited to models with low masses ($< 12 M_{\odot}$) near to the end of this evolutionary phase. For example, for a gravity, $\log g \sim 3.8$ dex (which is less than the median gravity for our B-type sample of 3.95 dex) changes are less than 5% with the rotational velocity having increased in some cases. Hence environmental effects such as those discussed by Wolff et al. (2007) could also be important.

However these results must be treated with some caution. K–S tests (using the same procedure for $v_e \sin i$ upper limits as in Sect. 5.3.2) for the samples in inner and outer regions of NGC 346 returned P-values of 16% (PF estimates) and 20% (FT estimates). Tests using samples for the inner region of NGC 346 and NGC 330 also returned high probabilities that they originated from the same populations. Hence we conclude that our SMC results are consistent with the Galactic investigations, although our samples remain too small to have a high level of statistical significance.

5.3.4. The rapidly rotating targets, #1134 and #1174

Two targets, #1134 and #1174, have estimates of their projected rotational velocity from the He I line at 4026 Å in excess of 500 km s^{-1} (see Table A.2). As discussed by, for example, Dufton et al. (2011), it is difficult to reliably estimate such large values due to the line profiles becoming very broad and shallow. We have therefore also obtained FT estimates from the other diffuse He I lines at 4143, 4387 and 4471 Å. These lead to mean values of 519 ± 15 (#1134) and 508 ± 17 (#1174) in reasonable agreement with the estimates from the 4026 Å line.

Irrespective of the precise values, it is clear that these stars have significantly greater projected rotational velocities than the rest of the sample. Adopting the effective temperatures, luminosities and masses estimated in Table A.2 and the SMC grid of evolutionary models of Brott et al. (2011a) leads to estimates of the critical velocity of 736 km s^{-1} (#1134) and 724 km s^{-1} (#1174), assuming an initial equatorial rotational velocity, $v_i \simeq 530 \text{ km s}^{-1}$. These critical velocities are relatively insensitive to the initial rotational velocity with a change of less than 10 km s^{-1} for the models with $v_i \simeq 590 \text{ km s}^{-1}$. In turn, this implies that both stars are rotating at more than 70% of the critical velocity. Indeed, given that the average values for $\sin i$ assuming a random distribution of inclination axes is 0.785 (Gray 2005), it is possible that both stars are rotating at near critical velocities.

Dufton et al. (2011) previously discussed an LMC star, VFTS 102 with a spectral type O9: Vnnne and a projected rotational velocity, $v_e \sin i = 600 \pm 100 \text{ km s}^{-1}$, lying approximately 12 pc from the X-ray pulsar PSR J0537–6910 in the plane of the sky. They suggested that this object originated from a binary system with its high projected rotational velocity resulting from mass transfer from the progenitor of PSR J0537–691. We have therefore searched for pulsars and supernova remnants (SNRs) in the vicinity of #1134 and #1174.

The closest pulsar in the ATNF Pulsar Catalogue⁹ (Manchester et al. 2005) is PSR J0100–7211, identified by Lamb et al. (2002) as an anomalous X-ray pulsar. Subsequently, Durant & van Kerkwijk (2005) identified a *possible* optical counterpart from *HST* imaging but this was not confirmed from further deep imaging with the *HST*. Its X-ray properties were discussed by McGarry et al. (2005), who found a characteristic age of ($P/2\dot{P}$)

⁹An updated version of this catalogue is available from: <http://www.atnf.csiro.au/research/pulsar/psrcat>

of 6800 yr. Both #1134 and #1174 lie approximately 0.15° from the pulsar corresponding to approximately 160 pc at the distance of the SMC. Adopting the characteristic age would then require a relative velocity in excess of $23\,000 \text{ km s}^{-1}$ for them to have previously been physically connected. Hence we conclude that it is highly unlikely that either star were physically associated with the progenitor of PSR J0100–7211. This is confirmed by their proper motion estimates (see Table 5), which are consistent with the median values for NGC 346. Similar arguments would apply to other SMC pulsars, although we note that their beamed emission implies that other such objects may lie closer to our two targets but remain undetected at present.

The nearest catalogued supernova remnant to either target is B0057–72.2 (also designated B0057–72.4). The position found by Filipović et al. (2002) from radio observations leads to angular separations of $3'.7$ (#1134) and $5'.7$ (#1174), which correspond to sky separations of approximately 65 and 100 pc respectively. However these distances must be treated with caution given the large angular size of the SNR. For example, Davies et al. (1976) from optical imaging found major and minor axes of $14'$ and $11'$ with evidence for sub-structure.

Given the large rotational velocities combined with the Be nature of both targets (and nebular contamination in #1134) it was difficult to recover robust estimates of their radial velocities. Nonetheless, estimates from the He I lines are not inconsistent with what we would expect for the region (cf. results from Evans et al. 2006), i.e. they do not appear to be significantly offset from the local systemic value, suggesting neither is a significant (RV) runaway.

In summary, there is no direct evidence that either of these targets originated from a binary system where their companion became a supernova. However, we cannot discount that they were originally the secondary components of a binary system. Mass transfer from the primary would then lead to their rapid rotation and their characterisation as a single star as discussed by, for example, de Mink et al. (2013, 2014) and Boubert & Evans (2018). Although their evolutionary pathways remain unclear, their projected rotational velocities suggest that they may have had a different evolutionary history to the rest of our sample.

5.3.5. Metallicity effects

Our projected rotational velocity estimates can be compared with those found from the VFTS to search for effects due to the different metallicities of the Clouds. The VFTS spectroscopy was obtained with same instrumentation to that used here, while the data reduction and analysis methodologies were similar. Therefore, we do not expect any major systematic differences between estimates from the two datasets.

Estimates for the O-type single and binary targets were obtained by Ramírez-Agudelo et al. (2013, 2015), with those for the B-type samples being taken from Dufton et al. (2013) and Garland et al. (2017). We have limited our comparison to samples of hydrogen core burning objects (i.e. excluding luminosity classes I and II). In Figure 6, we display the CPD for our largest sub-sample of single B-type stars, together with those for the same cohort in 30 Doradus (Dufton et al. 2013).

The distributions are similar although there is some evidence for the B-type stars in 30 Doradus having higher rotational velocities. In part, this may reflect a higher fraction of this sample being associated with clusters (Evans et al. 2011). This would be consistent with the median projected rotational velocity (see Table 6) for 30 Doradus being in good agreement with that for

Table 7. Statistical tests on the estimated projected rotational velocities for main-sequence (MS) stars in the NGC 346 (346), VFTS (30 Dor) and NGC 6611 (6611) samples. The first four columns identify the samples and the number of estimates. For the B-type samples, targets classified later than B3 were excluded. The latter four columns list the D-statistic and probability that the two samples come from the same parent population (P) for the Kolmogorov–Smirnov (K–S) and Kuiper tests.

Sample	Number			K–S		Kuiper	
	346	30 Dor	6611	D	P	D	P
Single MS O-type	34	189	–	0.117	0.804	0.159	0.936
Binary MS O-type	9	104	–	0.154	0.981	0.253	0.982
Single MS B-type	218	289	–	0.119	0.055	0.133	0.173
Binary MS B-type	40	95	–	0.203	0.175	0.272	0.178
Single MS B-type	218	–	24	0.210	0.262	0.351	0.063

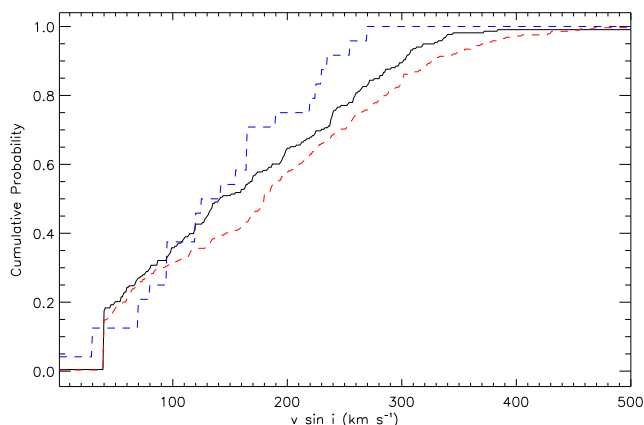


Fig. 6. Cumulative probability distributions for the single B-type stars in NGC 346 (black line), 30 Doradus (red dotted line), NGC 6611 (blue dotted line). Upper limits on $v_e \sin i$ estimates have been set to 40 km s^{-1} .

the inner region of NGC 346 but larger than those for the field dominated sample.

We have investigated this further using statistical tests for the four sub-samples of the O- and B-type targets split into apparently single and binary systems. K–S and Kuiper tests were performed and the results are summarized in Table 7. For all cases, there is no evidence that the projected rotational velocity distributions in NGC 346 and 30 Doradus are different at a 5% significance level. In turn this implies that there is no evidence for the rotational velocity distributions being different in the two metallicity environments.

For completeness, in Fig. 6 we also show the CPD for the projected rotational velocity estimates of B-type stars in NGC 6611 based on the FSMS observations (Dufton et al. 2006b) and list the median value in Table 6. The CPD implies that the NGC 6611 targets have, on average, lower rotational rates, which is supported by its lower median. As the NGC 6611 targets should be all cluster members, this would be consistent with faster rotation occurring in lower metallicity environments. However the statistical tests summarized in Table 7 show that these differences are not significant at a 5% level, due to the relatively small sample size for NGC 6611.

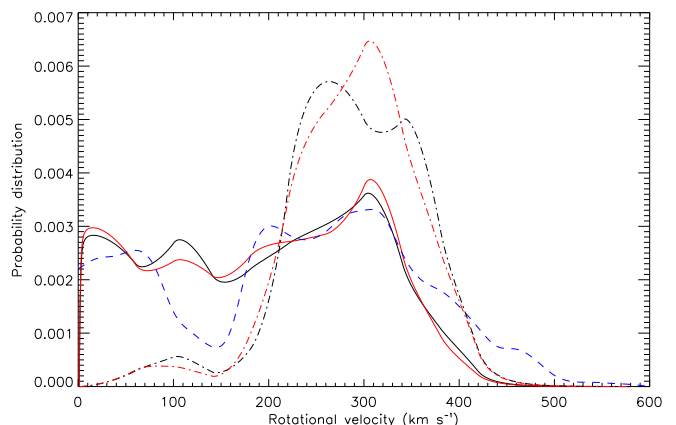


Fig. 7. Rotational velocity probability distributions, $f(v_e)$, for the apparently single B-type stars in NGC 346 deduced from the PF (black line) and FT (red line) estimates, and for the equivalent sample in 30 Doradus (dotted blue line) of Dufton et al. (2013). Also shown are the equivalent distributions for the apparently single Be-type (dash-dotted black and red lines).

5.3.6. Deconvolution of the $v_e \sin i$ distribution

Our sample of apparently single non-supergiant B-type targets is large enough to estimate the current distribution of their rotational velocities. Assuming that their rotation axes are randomly distributed, we can infer the probability density function distribution, $P(v_e)$, using the iterative procedure of Lucy (1974) as implemented by Dufton et al. (2013), where further details can be found. The two extremely fast rotators (#1134 and #1174) have been excluded from the deconvolution for numerical stability reasons.

The probability distributions implied by both the FT and PF $v_e \sin i$ estimates are shown in Fig. 7, together with that for the equivalent sample in the 30 Doradus region (Dufton et al. 2013). The two probability distributions inferred for the NGC 346 are broadly similar, reflecting the good agreement between the PF and FT estimates as discussed in Sect. 4.2.

As discussed in Sect. 5.3.5, the CDFs for the $v_e \sin i$ estimates of NGC 346 and 30 Doradus were consistent with them having the same parent population and this must be borne in mind when considering possible differences. In general, the distributions are similar with a significant population of stars having small rotational velocities and with a second maximum at approximately 300 km s^{-1} . The NGC 346 sample has some ad-

ditional structure between 80 and 200 km s⁻¹ but given the differences between the two $P(v_e)$ distributions based on the PF and FT estimates, this cannot be considered significant. Additionally, as discussed by Dufton et al. (2013), the use of a bin size of 40 km s⁻¹ in the de-convolution implies that structure on this scale or smaller is unlikely to be real. There may also be differences at high rotational velocities ($v_e > 350$ km s⁻¹) but given the relatively small number of targets with large projected rotational velocities (see Fig. 6), these can again not be considered significant.

For both regions approximately 10% of the targets have rotational velocities of less than 40 km s⁻¹. For 30 Doradus, Dufton et al. (2018) found that a significant fraction of these targets had enhanced nitrogen abundances that were inconsistent with current single star evolutionary models. They considered possible explanations, of which the most promising would appear to be braking due to magnetic fields (Morel 2012; Aerts et al. 2014) or stellar mergers with subsequent magnetic braking (Schneider et al. 2016). A similar investigation of the B-type stars in NGC 346 would be valuable.

Our best estimates of the probability density function for the apparently single B-type stars (excluding supergiants) are given in Table 8. These values require a judgement about the nature of the smaller scale structure as discussed above. Also listed is the cumulative distribution function corresponding to these estimates and, because this is truncated at $v_e \leq 500$ km s⁻¹, it does not reach unity. We recommend that either the range up to the critical velocity is populated or that the probability density function is renormalised, depending on the nature of the application.

5.3.7. Rotational velocities of the Be-type stars

Classical Be-type stars have prominent emission features in their Balmer line spectrum, indicating the presence of a geometrically flattened, circumstellar disc (Quirrenbach et al. 1994, 1997). Zorec & Briot (1997) have estimated that approximately 17% of Galactic stars showed the Be phenomenon, with the highest fraction around B1e–B2e. Emission is also often seen in the helium and iron spectra, with silicon and magnesium emission lines being seen in some stars Porter & Rivinius (2003). A recent review of the Be phenomenon has been given by Rivinius et al. (2013)

Seventy three targets have been identified as Be-type equating to 25% of the total B-type sample; this increases to 27% if supergiants are excluded. Nine of the Be-type stars are binaries and excluding these leads to 29% of the apparently single stars (excluding supergiants) being Be-type. These percentages are higher than those found by Zorec & Briot (1997, 17%) for Galactic field stars and by Martayan et al. (2006b, 18%) towards NGC 2004 in the LMC (this sample was predominantly field stars). Our Be-type percentages are similar to that of Martayan et al. (2007, 26%) for the field towards NGC 330 and Bonanos et al. (2010, 27%) from an infrared investigations of the SMC. Martayan et al. (2006b, 2007) found tentative evidence that the proportion of Be-type stars in clusters might be higher but these were based on small numbers of B-type stars (LMC: 19 stars, SMC: 18 stars). For our sample of 33 apparently single B-type stars within 2'0 of the centre of NGC 346, we find 6 Be-type stars (excluding #1100 which is possibly a Herbig B-star) leading to a percentage of 18%, with an upper 95% confidence limit of 33%. Hence although there is no evidence for an increased Be-type fraction in the centre of NGC 346, our sample is too small to exclude that possibility

The mechanisms underlying the Be phenomenon remain unclear but such stars in our Galaxy are believed to be fast rotators

Table 8. Estimates of the probability density of the rotational velocity, $P(v_e)$, and its cumulative distribution function (cdf) for the NGC 346 apparently single B-type sample. Supergiants (luminosity classes I and II) were excluded from the de-convolution.

v_e	$P(v_e) \times 10^3$	cdf
0	2.90	0.0000
20	2.90	0.0580
40	2.75	0.1145
60	2.40	0.1660
80	2.25	0.2125
100	2.20	0.2570
120	2.15	0.3005
140	2.15	0.3435
160	2.20	0.3870
180	2.25	0.4315
200	2.45	0.4785
220	2.60	0.5290
240	2.80	0.5830
260	2.95	0.6405
280	3.10	0.7010
300	3.60	0.7680
320	3.50	0.8390
340	2.55	0.8995
360	1.70	0.9420
380	1.00	0.9690
400	0.60	0.9850
420	0.25	0.9935
440	0.10	0.9970
460	0.05	0.9985
480	0.02	0.9992
500	0.00	0.9994

with velocities that range from ~60% up to 100% (Chauville et al. 2001; Frémat et al. 2005; Cranmer 2005; Rivinius et al. 2006; Ekström et al. 2008) of the critical limit (Townsend et al. 2004). For our sample, this is consistent with the small number of Be-type stars with low $v_e \sin i$ estimates and a correspondingly large median value of 240 km s⁻¹ compared with those in Table 6. For the apparently single Be-type stars, we have performed a de-convolution of the $v_e \sin i$ estimates using the same methodology as summarized in Sect. 5.3.6. In Fig. 7, these are shown for both the PF and FT $v_e \sin i$ estimates. The sample size is small and hence caution should be exercised in interpreting these results. For example, there appears to be a population of slowly rotating Be-type stars ($v_e \sim 100$ km s⁻¹) but this is based on a relatively small number (9-10) of targets with correspondingly low $v_e \sin i$ estimates.

The rotational velocities of our Be-type sample mainly lie in the range ~200–450 km s⁻¹. Dunstall et al. (2011) inferred rotational velocity distributions for Be-type samples in the Magellanic Clouds assuming a Gaussian distribution. For the SMC, these peaked at rotational velocities of 260 km s⁻¹ and 310 km s⁻¹ for the FSMS and the survey of Martayan et al. (2006a) respectively in good agreement with the results found here. Adopting the critical velocity estimates from Sect. 5.3.4 would then imply that they are rotating at ~0.3–0.6 of this velocity. This is lower than that generally found for Galactic targets but as discussed by Rivinius et al. (2013), there may be systematic biases in our $v_e \sin i$ estimates. These would include addi-

tional absorption in shell stars and line emission in Be stars, as well as the presence (of a presumably narrower lined) secondary.

In summary, the projected rotational velocities of our Be-type stars are systematic larger than those of the rest of the B-type stars. This implies rotational velocities between 200–450 km s⁻¹, although the Be-type velocities may be subject to systematic biases.

6. Conclusions

We have presented spectral types and estimates of the atmospheric parameters and projected rotational velocities for the hot star population towards NGC 346. Additionally, we have inferred masses and ages using the BONNSAI package (Schneider et al. 2014). Our conclusions are:

1. Targets towards the inner region of NGC 346 have higher median masses and smaller ages than the rest of the sample. There appears to be a population of very young targets with ages of less than 2 Myr. These are predominantly in the inner region, while the three young targets at greater radial distances could also have been formed nearer the centre.
2. The more massive targets may have lower median projected rotational velocities consistent with previous studies of the Magellanic Clouds.
3. Targets close to the centre of NGC 346 have a higher mean projected rotational velocities than those at larger radial distances consistent with previous Galactic studies.
4. Two targets (#1134 and #1174) have very large projected rotational velocities and are rotating in excess of 70% of their critical velocities. Their origin is investigated and especially whether they could be the original secondaries in a binary where the primary evolved into a supernova. However it is not possible to draw firm conclusions from the current observations.
5. A comparison with the 30 Doradus region in the LMC finds no evidence for significant differences in early-type stellar rotational velocities with metallicity. There is some evidence that the SMC targets rotate faster than those in young Galactic clusters but this is not statistically significant. These results agree with the conclusions from ultraviolet studies of early-type stars in the Clouds (Penny et al. 2004; Penny & Gies 2009).
6. The projected rotational velocities for the apparently single B-type hydrogen burning targets have been deconvolved to infer their rotational velocity distribution. This shows that a significant number have low rotational velocities ($\approx 10\%$ with $v_e < 40$ km s⁻¹). Additionally the distribution peaks at a rotational velocity of approximately 300 km s⁻¹.
7. Relatively large projected rotational velocity have been found for our Be-type sample and imply rotational velocities between 200–450 km s⁻¹. As our Be-type $v_e \sin i$ estimates may be systematically biased to lower values, this difference between the rotational velocities of the B-type and Be-type stars may be even larger.

The results presented here are based on samples of approximately 350 and 750 targets in the SMC and LMC respectively. Further progress in understanding the rotational velocities of

early-type stars in the Magellanic Clouds will require significantly larger samples of targets. Additionally it will be important to ensure that the samples are well constrained in both their spatial position (field or cluster) and their physical parameters (binarity, mass, age etc.).

Acknowledgements. Based on observations at the European Southern Observatory in programme 074D.0011 and 171.D-0237. This work has made use of data from the European Space Agency (ESA) mission *Gaia* (<https://www.cosmos.esa.int/gaia>), processed by the *Gaia* Data Processing and Analysis Consortium (DPAC, <https://www.cosmos.esa.int/web/gaia/dpac/consortium>). Funding for the DPAC has been provided by national institutions, in particular the institutions participating in the *Gaia* Multilateral Agreement. CJE and DJL acknowledge the OWC. CJE thanks Linda Smith for obtaining the AAT spectra, and is grateful for the past hospitality of the Space Telescope Science Institute and travel funding from its Director's Discretionary Research Fund (DDRF).

References

- Aerts, C., Molenberghs, G., Kenward, M. G., & Neiner, C. 2014, *ApJ*, 781, 88
 Azzopardi, M. & Vigneanu, J. 1975, *A&AS*, 19, 271
 Azzopardi, M. & Vigneanu, J. 1982, *A&AS*, 50, 291
 Balona, L. A. 1994, *MNRAS*, 268, 119
 Bica, E. L. D. & Schmitt, H. R. 1995, *ApJS*, 101, 41
 Blecha, A., North, P., Royer, F., & Simond, G. 2003, *BLDR Software - Reference Manual*, 1st edn.
 Bonanos, A. Z., Lennon, D. J., Köhlinger, F., et al. 2010, *AJ*, 140, 416
 Boubert, D. & Evans, N. W. 2018, *MNRAS*, 477, 5261
 Bouchet, P., Lequeux, J., Maurice, E., Prevot, L., & Prevot-Burnichon, M. L. 1985, *A&A*, 149, 330
 Bouret, J., Lanz, T., Hillier, D. J., et al. 2003, *ApJ*, 595, 1182
 Bouret, J.-C., Lanz, T., Martins, F., et al. 2013, *A&A*, 555, A1
 Brott, I., de Mink, S. E., Cantiello, M., et al. 2011a, *A&A*, 530, A115
 Brott, I., Evans, C. J., Hunter, I., et al. 2011b, *A&A*, 530, A116
 Carroll, J. A. 1933, *MNRAS*, 93, 478
 Chauville, J., Zorec, J., Ballereau, D., et al. 2001, *A&A*, 378, 861
 Cignoni, M., Tosi, M., Sabbi, E., Nota, A., & Gallagher, J. S. 2011, *AJ*, 141, 31
 Cranmer, S. R. 2005, *ApJ*, 634, 585
 Currie, M. J., Berry, D. S., Jenness, T., et al. 2014, in *Astronomical Data Analysis Software and Systems XXIII*, Vol. 485, 391
 Davies, R. D., Elliott, K. H., & Meaburn, J. 1976, *Memoirs of the Royal Astronomical Society*, 81, 89
 de Mink, S. E., Langer, N., Izzard, R. G., Sana, H., & de Koter, A. 2013, *ApJ*, 764, 166
 de Mink, S. E., Sana, H., Langer, N., Izzard, R. G., & Schneider, F. R. N. 2014, *ApJ*, 782, 7
 Dufton, P. L., Dunstall, P. R., Evans, C. J., et al. 2011, *ApJ*, 743, L22
 Dufton, P. L., Langer, N., Dunstall, P. R., et al. 2013, *A&A*, 550, A109
 Dufton, P. L., Ryans, R. S. I., Simón-Díaz, S., Trundle, C., & Lennon, D. J. 2006a, *A&A*, 451, 603
 Dufton, P. L., Ryans, R. S. I., Trundle, C., et al. 2005, *A&A*, 434, 1125
 Dufton, P. L., Smartt, S. J., Lee, J. K., et al. 2006b, *A&A*, 457, 265
 Dufton, P. L., Thompson, A., Crowther, P. A., et al. 2018, *A&A*, 615, A101
 Dunstall, P. R., Brott, I., Dufton, P. L., et al. 2011, *A&A*, 536, A65
 Dunstall, P. R., Dufton, P. L., Sana, H., et al. 2015, *A&A*, 580, A93
 Durant, M. & van Kerkwijk, M. H. 2005, *ApJ*, 628, L135
 Ekström, S., Meynet, G., Maeder, A., & Barblan, F. 2008, *A&A*, 478, 467
 Evans, C. J. & Howarth, I. D. 2003, *MNRAS*, 345, 1223
 Evans, C. J., Howarth, I. D., Irwin, M. J., Burnley, A. W., & Harries, T. J. 2004, *MNRAS*, 353, 601
 Evans, C. J., Lennon, D. J., Smartt, S. J., & Trundle, C. 2006, *A&A*, 456, 623
 Evans, C. J., Smartt, S. J., Lee, J.-K., et al. 2005, *A&A*, 437, 467
 Evans, C. J., Taylor, W. D., Hénault-Brunet, V., et al. 2011, *A&A*, 530, A108
 Fasano, G. & Franceschini, A. 1987, *MNRAS*, 225, 155
 Filipović, M. D., Bohlsen, T., Reid, W., et al. 2002, *MNRAS*, 335, 1085
 Fraser, M., Dufton, P. L., Hunter, I., & Ryans, R. S. I. 2010, *MNRAS*, 404, 1306
 Frémat, Y., Zorec, J., Hubert, A.-M., & Floquet, M. 2005, *A&A*, 440, 305
 Gaia Collaboration, Brown, A. G. A., Vallenari, A., et al. 2018, *A&A*, 616, A1
 Gaia Collaboration, Prusti, T., de Bruijne, J. H. J., et al. 2016, *A&A*, 595, A1
 Garland, R., Dufton, P. L., Evans, C. J., et al. 2017, *A&A*, 603, A91
 Garmany, C. D., Conti, P. S., & Massey, P. 1987, *AJ*, 93, 1070
 Georgy, C., Ekström, S., Eggenberger, P., et al. 2013a, *A&A*, 558, A103
 Georgy, C., Ekström, S., Granada, A., et al. 2013b, *A&A*, 553, A24
 Getman, K. V., Feigelson, E. D., & Kuhn, M. A. 2014a, *ApJ*, 787, 109
 Getman, K. V., Feigelson, E. D., Kuhn, M. A., et al. 2018, *MNRAS*, 476, 1213
 Getman, K. V., Feigelson, E. D., Kuhn, M. A., et al. 2014b, *ApJ*, 787, 108

- Gies, M. & Portegies Zwart, S. F. 2011, *MNRAS*, 410, L6
- Gies, D. R. & Lambert, D. L. 1992, *ApJ*, 387, 673
- Gouliermis, D. A., Chu, Y.-H., Henning, T., et al. 2008, *ApJ*, 688, 1050
- Gouliermis, D. A., Hony, S., & Klessen, R. S. 2014, *MNRAS*, 439, 3775
- Gray, D. F. 2005, *The Observation and Analysis of Stellar Photospheres*
- Grin, N. J., Ramírez-Agudelo, O. H., de Koter, A., et al. 2017, *A&A*, 600, A82
- Hanuschik, R. W., Hummel, W., Dietle, O., & Sutorius, E. 1995, *A&A*, 300, 163
- Harries, T. J., Hilditch, R. W., & Howarth, I. D. 2003, *MNRAS*, 339, 157
- Heap, S. R., Lanz, T., & Hubeny, I. 2006, *ApJ*, 638, 409
- Heger, A. & Langer, N. 2000, *ApJ*, 544, 1016
- Henize, K. G. 1956, *ApJS*, 2, 315
- Hennekemper, E., Gouliermis, D. A., Henning, T., Brandner, W., & Dolphin, A. E. 2008, *ApJ*, 672, 914
- Herrero, A., Kudritzki, R. P., Vilchez, J. M., et al. 1992, *A&A*, 261, 209
- Heydari-Malayeri, M. & Hutsemekers, D. 1991, *A&A*, 243, 401
- Heydari-Malayeri, M. & Selier, R. 2010, *A&A*, 517, A39
- Hilditch, R. W., Howarth, I. D., & Harries, T. J. 2005, *MNRAS*, 357, 304
- Huang, W. & Gies, D. R. 2006, *ApJ*, 648, 580
- Hubeny, I. 1988, *Computer Physics Communications*, 52, 103
- Hubeny, I., Heap, S. R., & Lanz, T. 1998, in *Astronomical Society of the Pacific Conference Series*, Vol. 131, *Properties of Hot Luminous Stars*, ed. I. Howarth, 108
- Hubeny, I. & Lanz, T. 1995, *ApJ*, 439, 875
- Humphreys, R. M. 1983, *ApJ*, 265, 176
- Hunter, I., Brott, I., Langer, N., et al. 2009, *A&A*, 496, 841
- Hunter, I., Brott, I., Lennon, D. J., et al. 2008a, *ApJ*, 676, L29
- Hunter, I., Dufton, P. L., Smartt, S. J., et al. 2007, *A&A*, 466, 277
- Hunter, I., Lennon, D. J., Dufton, P. L., et al. 2008b, *A&A*, 479, 541
- Indu, G. & Subramaniam, A. 2011, *A&A*, 535, A115
- Keller, S. C. 2004, *PASA*, 21, 310
- Keller, S. C., Wood, P. R., & Bessell, M. S. 1999, *A&AS*, 134, 489
- Koenigsberger, G., Morrell, N., Hillier, D. J., et al. 2014, *AJ*, 148, 62
- Korn, A. J., Keller, S. C., Kaufer, A., et al. 2002, *A&A*, 385, 143
- Korn, A. J., Nieva, M. F., Daflon, S., & Cunha, K. 2005, *ApJ*, 633, 899
- Kudritzki, R. P., Pauldrach, A., & Puls, J. 1987, *A&A*, 173, 293
- Kudritzki, R.-P. & Puls, J. 2000, *ARA&A*, 38, 613
- Lamb, R. C., Fox, D. W., Macomb, D. J., & Prince, T. A. 2002, *ApJ*, 574, L29
- Lanz, T. & Hubeny, I. 2003, *ApJS*, 146, 417
- Lanz, T. & Hubeny, I. 2007, *ApJS*, 169, 83
- Lefever, K., Puls, J., & Aerts, C. 2007, *A&A*, 463, 1093
- Lennon, D. J. 1997, *A&A*, 317, 871
- Lennon, D. J., Dufton, P. L., & Crowley, C. 2003, *A&A*, 398, 455
- Lucy, L. B. 1974, *AJ*, 79, 745
- Maeder, A. & Meynet, G. 2001, *A&A*, 373, 555
- Maeder, A., Przybilla, N., Nieva, M.-F., et al. 2014, *A&A*, 565, A39
- Manchester, R. N., Hobbs, G. B., Teoh, A., & Hobbs, M. 2005, *AJ*, 129, 1993
- Markova, N. & Puls, J. 2008, *A&A*, 478, 823
- Markova, N., Puls, J., & Langer, N. 2018, *A&A*, 613, A12
- Martayan, C., Floquet, M., Hubert, A. M., et al. 2007, *A&A*, 472, 577
- Martayan, C., Frémat, Y., Hubert, A., et al. 2006a, *A&A*, 452, 273
- Martayan, C., Hubert, A. M., Floquet, M., et al. 2006b, *A&A*, 445, 931
- Massey, P., Lang, C. C., Degioia-Eastwood, K., & Garmany, C. D. 1995, *ApJ*, 438, 188
- Massey, P., Morrell, N. I., Neugent, K. F., et al. 2012, *ApJ*, 748, 96
- Massey, P., Parker, J. W., & Garmany, C. D. 1989, *AJ*, 98, 1305
- Massey, P., Zangari, A. M., Morrell, N. I., et al. 2009, *ApJ*, 692, 618
- McGarry, M. B., Gaensler, B. M., Ransom, S. M., Kaspi, V. M., & Veljkovic, S. 2005, *ApJ*, 627, L137
- Mennickent, R. E. & Smith, M. A. 2010, *MNRAS*, 407, 734
- Meynet, G. & Maeder, A. 2000, *A&A*, 361, 101
- Meynet, G. & Maeder, A. 2005, *A&A*, 429, 581
- Meyssonnier, N. & Azzopardi, M. 1993, *A&AS*, 102, 451
- Mokiem, M. R., de Koter, A., Evans, C. J., et al. 2006, *A&A*, 456, 1131
- Mokiem, M. R., de Koter, A., Vink, J. S., et al. 2007, *A&A*, 473, 603
- Momany, Y., Vandame, B., Zaggia, S., et al. 2001, *A&A*, 379, 436
- Morel, T. 2012, in *Astronomical Society of the Pacific Conference Series*, Vol. 465, *Proceedings of a Scientific Meeting in Honor of Anthony F. J. Moffat*, ed. L. Drissen, C. Robert, N. St-Louis, & A. F. J. Moffat, 54
- Niemela, V. & Gamen, R. 2004, *New A Rev.*, 48, 727
- Niemela, V. S. 2002, in *IAU Symposium*, Vol. 207, *Extragalactic Star Clusters*, ed. D. P. Geisler, E. K. Grebel, & D. Minniti, 202
- Niemela, V. S., Marraco, H. G., & Cabanne, M. L. 1986, *PASP*, 98, 1133
- Pasquini, L., Avila, G., Blecha, A., et al. 2002, *The Messenger*, 110, 1
- Pawlak, M., Graczyk, D., Soszyński, I., et al. 2013, *Acta Astron.*, 63, 323
- Penny, L. R. & Gies, D. R. 2009, *ApJ*, 700, 844
- Penny, L. R., Sprague, A. J., Seago, G., & Gies, D. R. 2004, *ApJ*, 617, 1316
- Porter, J. M. & Rivinius, T. 2003, *PASP*, 115, 1153
- Quirrenbach, A., Bjorkman, K. S., Bjorkman, J. E., et al. 1997, *ApJ*, 479, 477
- Quirrenbach, A., Buscher, D. F., Mozurkewich, D., Hummel, C. A., & Armstrong, J. T. 1994, *A&A*, 283, L13
- Ramírez-Agudelo, O. H., Sana, H., de Koter, A., et al. 2017, *A&A*, 600, A81
- Ramírez-Agudelo, O. H., Sana, H., de Mink, S. E., et al. 2015, *A&A*, 580, A92
- Ramírez-Agudelo, O. H., Simón-Díaz, S., Sana, H., et al. 2013, *A&A*, 560, A29
- Relaño, M., Peimbert, M., & Beckman, J. 2002, *ApJ*, 564, 704
- Ritchie, B. W., Stroud, V. E., Evans, C. J., et al. 2012, *A&A*, 537, A29
- Rivero González, J. G., Puls, J., Najarro, F., & Brott, I. 2012, *A&A*, 537, A79
- Rivinius, T., Carciofi, A. C., & Martayan, C. 2013, *A&A Rev.*, 21, 69
- Rivinius, T., Stefl, S., & Baade, D. 2006, *A&A*, 459, 137
- Rochau, B., Gouliermis, D. A., Brandner, W., Dolphin, A. E., & Henning, T. 2007, *ApJ*, 664, 322
- Ryans, R. S. I., Dufton, P. L., Mooney, C. J., et al. 2003, *A&A*, 401, 1119
- Ryans, R. S. I., Dufton, P. L., Rolleston, W. R. J., et al. 2002, *MNRAS*, 336, 577
- Sabbi, E., Sirianni, M., Nota, A., et al. 2007, *AJ*, 133, 44
- Sabbi, E., Sirianni, M., Nota, A., et al. 2008, *AJ*, 135, 173
- Salpeter, E. E. 1955, *ApJ*, 121, 161
- Sana, H., de Koter, A., de Mink, S. E., et al. 2013, *A&A*, 550, A107
- Sanduleak, N. 1968, *AJ*, 73, 246
- Schneider, F. R. N., Castro, N., Fossati, L., Langer, N., & de Koter, A. 2017, *A&A*, 598, A60
- Schneider, F. R. N., Langer, N., de Koter, A., et al. 2014, *A&A*, 570, A66
- Schneider, F. R. N., Podsiadlowski, P., Langer, N., Castro, N., & Fossati, L. 2016, *MNRAS*, 457, 2355
- Schneider, F. R. N., Ramírez-Agudelo, O. H., Tramper, F., et al. 2018, *A&A*, 618, A73
- Simón-Díaz, S., Godart, M., Castro, N., et al. 2017, *A&A*, 597, A22
- Simón-Díaz, S. & Herrero, A. 2007, *A&A*, 468, 1063
- Simón-Díaz, S. & Herrero, A. 2014, *A&A*, 562, A135
- Simón-Díaz, S., Herrero, A., Uytterhoeven, K., et al. 2010, *ApJ*, 720, L174
- Strom, S. E., Wolff, S. C., & Dror, D. H. A. 2005, *AJ*, 129, 809
- Townsend, R. H. D., Owocki, S. P., & Howarth, I. D. 2004, *MNRAS*, 350, 189
- Trundle, C., Dufton, P. L., Hunter, I., et al. 2007, *A&A*, 471, 625
- Udalski, A., Soszynski, I., Szymanski, M., et al. 1998, *Acta Astron.*, 48, 563
- Vacca, W. D., Garmany, C. D., & Shull, J. M. 1996, *ApJ*, 460, 914
- Venn, K. A. 1999, *ApJ*, 518, 405
- Vink, J. S. & de Koter, A. 2005, *A&A*, 442, 587
- Walborn, N. R. 1970, *ApJ*, 161, L149
- Walborn, N. R. 1972, *AJ*, 77, 312
- Walborn, N. R. 1978, *ApJ*, 224, L133
- Walborn, N. R. & Blades, J. C. 1986, *ApJ*, 304, L17
- Walborn, N. R., Howarth, I. D., Lennon, D. J., et al. 2002, *AJ*, 123, 2754
- Walborn, N. R., Lennon, D. J., Haser, S. M., Kudritzki, R.-P., & Voels, S. A. 1995, *PASP*, 107, 104
- Walborn, N. R., Lennon, D. J., Heap, S. R., et al. 2000, *PASP*, 112, 1243
- Wisniewski, J. P., Bjorkman, K. S., Magalhães, A. M., et al. 2007, *ApJ*, 671, 2040
- Wolff, S. C., Strom, S. E., Cunha, K., et al. 2008, *AJ*, 136, 1049
- Wolff, S. C., Strom, S. E., Dror, D., & Venn, K. 2007, *AJ*, 133, 1092
- Woosley, S. E. & Heger, A. 2006, *ApJ*, 637, 914
- Wyrzykowski, L., Udalski, A., Kubiak, M., et al. 2004, *Acta Astron.*, 54, 1
- Yoon, S.-C. & Langer, N. 2005, *A&A*, 443, 643
- Zorec, J. & Briot, D. 1997, *A&A*, 318, 443

Appendix A: Data Tables

Table A.1. Observational parameters of target stars. Cross-references to previous identifications are given in the final column as follows: Sanduleak (1968, Sk), Azzopardi & Vigneau (1975, 1982, AzV), Walborn & Blades (1986, WB), Niemela et al. (1986, NMC), Massey et al. (1989, MPG), Meyssonnier & Azzopardi (1993, MA93), Keller et al. (1999, KWB), and Evans et al. (2004, 2dFS). Additionally eclipsing binaries (EB) from the OGLE project (Udalski et al. 1998) have been identified. Radial distances from #1001 (r_d , in arcmin) are given for each star (1' corresponds to a physical distance of ~ 17.5 pc).

ID	$\alpha(2000)$	$\delta(2000)$	r_d	V	$B - V$	Spectral Type	Comments
1001	00 59 04.49	-72 10 24.7	0.00	12.61	-0.28	O4 If + O5-6	Binary (SB2); WB 1, NMC 26, MPG 435 – O5.5 If; †
1002	00 58 35.82	-72 16 24.8	6.39	12.80	0.01	B1.5 Ia	Sk 73, AzV 210; †; small v_r shifts of ~ 10 km s $^{-1}$
1003	00 59 43.46	-72 04 18.7	6.79	12.96	-0.14	B3 Iab	Sk 81, AzV 234; †
1004	00 57 05.45	-72 09 51.9	9.13	13.34	0.01	A2 Ib	
1005	00 57 04.09	-72 08 57.0	9.33	13.38	-0.02	A2 Ib	
1006	00 59 54.88	-72 13 06.3	4.70	13.40	-0.09	A2 Ib	MPG 859, 2dFS#5102 – B9 (Ib)
1007	00 58 54.80	-72 13 17.1	2.97	13.46	0.03	B1 Ia	Binary (SB1); AzV 214, MPG 293; †
1008	00 59 00.75	-72 10 28.1	0.29	13.52	-0.22	O2 III(f*)	WB 3, NMC 29, MPG 355 – O3 V(f*); †
1009	00 58 10.00	-72 11 01.8	4.22	13.59	-0.06	B1e	MA93#1061, KWB346#34
1010	00 59 00.05	-72 10 37.8	0.40	13.66	-0.26	O5-6 V((f))	Binary (SB3); WB 4, NMC 30, MPG 342 – O5.5 V+neb; †
1011	00 59 55.49	-72 13 37.7	5.06	13.77	-0.22	O9 III	Binary (SB1); AzV 238; †
1012	00 59 01.81	-72 10 31.1	0.23	14.21	-0.25	O6: V((f))	Binary (SB1); NMC 28, MPG 368; †
1013	00 59 06.34	-72 09 56.1	0.50	14.28	-0.15	B0.5e	NMC 37, MPG 482 – B0.5: V+neb, KWB346#85
1014	00 59 57.13	-72 07 52.5	4.76	14.39	-0.14	B3 Ib + mid A?	Binary (SB2?)
1015	00 59 02.92	-72 10 34.8	0.21	14.44	-0.24	O7 V	MPG 396 – O7 V
1016	00 59 36.51	-72 10 22.6	2.45	14.45	-0.08	B8 Ib	MPG 802
1017	01 00 16.07	-72 12 44.0	5.95	14.45	-0.26	O9 V	Binary (SB2); OGLE209964 (EB)
1018	00 57 00.71	-72 08 11.3	9.73	14.48	-0.11	B0 ne (shell)	AzV 182, 2dFS#1187 – B0 (III); †
1019	00 59 09.93	-72 05 48.2	4.63	14.48	-0.30	O6.5f?p	AzV 220, MA93#1121, KWB346#89; †
1020	00 59 06.86	-72 16 35.9	6.19	14.51	-0.19	B1 III	Binary (SB1); AzV 219, 2dFS#1363 – B1-3 (II)
1021	00 59 41.40	-72 08 10.4	3.60	14.63	-0.21	B2 II	
1022	00 57 55.22	-72 17 31.1	8.87	14.63	-0.06	B2 II	
1023	00 58 58.24	-72 13 46.5	3.40	14.64	-0.13	B0 V	Binary (SB1); OGLE110243 (EB)
1024	00 59 16.61	-72 12 10.0	1.99	14.64	0.05	A I + B?	MPG 665, MA93#1138, KWB346#93, OGLE160677 (EB)
1025	00 59 12.68	-72 11 09.1	0.97	14.66	-0.21	O7 V	MPG 615 – O8 V
1026	00 59 12.30	-72 11 07.9	0.94	14.70	-0.21	O6.5 V((f))	MPG 602
1027	00 58 17.40	-72 18 56.2	9.26	14.72	-0.06	B0-3e	MA93#1066
1028	00 58 02.99	-72 16 33.8	7.75	14.89	-0.16	B2.5 III	
1029	00 59 47.87	-72 04 50.8	6.48	14.89	-0.24	B2.5 III	
1030	00 59 15.51	-72 11 11.7	1.15	14.90	-0.26	OC5-6 Vz	MPG 655 – O6 V, KWB346#459; †
1031	00 58 42.72	-72 12 45.8	2.88	14.96	-0.12	B2-3e	MPG 184, MA93#1090, KWB346#171
1032	00 57 43.93	-72 04 32.5	8.51	14.99	-0.11	B0.5: e	
1033	00 59 06.01	-72 10 44.9	0.36	15.02	-0.25	B0 V	MPG 471 – B0 V+neb
1034	00 59 12.81	-72 10 52.3	0.79	15.02	-0.21	O9.5-B0 V	NMC 11, MPG 617 – O9.5 V
1035	00 59 03.97	-72 10 51.1	0.44	15.04	-0.26	O7.5 V((f))	MPG 417
1036	00 58 42.75	-72 14 28.2	4.39	15.05	-0.18	B2.5 III-II	2dFS#1333 – B2 (III)
1037	00 58 13.00	-72 15 35.3	6.51	15.06	-0.21	B0 III	2dFS#1295 – B0.5 (IV)
1038	00 58 50.25	-72 17 13.4	6.90	15.06	-0.01	B0: e	MA93#1104
1039	00 59 01.89	-72 10 43.2	0.37	15.06	-0.23	O9.5 V	Binary (SB1); MPG 370 – O9.5 V
1040	00 57 49.27	-72 16 55.3	8.69	15.07	-0.19	Early-B+Early-B	Binary (SB2); OGLE52815 (EB)
1041	00 58 19.34	-72 17 56.6	8.29	15.07	-0.33	B2 III-II	
1042	00 59 28.75	-72 10 16.6	1.86	15.12	-0.08	B1-2e	MPG 771 – B0 V+neb, MA93#1148, KWB346#248
1043	00 59 28.85	-72 12 31.7	2.82	15.14	-0.25	B0 V	MPG 770
1044	00 58 31.58	-72 18 21.0	8.33	15.15	-0.23	B1 III	2dFS#1320 – B1-3 (III)
1045	00 59 07.33	-72 10 25.3	0.22	15.17	-0.28	O9 V	Binary (SB1); NMC 24, MPG 495 – O8 V
1046	00 58 18.60	-72 04 26.9	6.92	15.20	-0.27	B0.5 V	
1047	00 57 51.15	-72 06 10.2	7.04	15.21	0.06	A5 III	2dFS#1267 – A3 II
1048	00 58 58.79	-72 10 51.3	0.62	15.21	-0.23	O9 V	MPG 330 – O7.5 V
1049	00 58 58.88	-72 10 38.8	0.49	15.21	-0.26	B0 V	Binary (SB2); NMC 31, MPG 332 – B0 V: +neb
1050	00 58 45.69	-72 17 16.6	7.02	15.22	-0.13	B1.5 II	2dFS#1337 – B1-2 (III)
1051	01 00 13.61	-72 12 44.6	5.78	15.22	-0.30	O9 V	
1052	00 59 05.44	-72 10 42.3	0.30	15.27	-0.22	B0 V	MPG 455; †
1053	00 57 41.17	-72 11 20.0	6.44	15.28	-0.19	B0.5 III	2dFS#1252 – B1-3 (III)
1054	01 00 06.44	-72 09 24.4	4.85	15.29	-0.29	B1 III	Binary (SB1)
1055	00 59 09.82	-72 10 59.0	0.70	15.32	-0.26	O9.5 V	NMC 13, MPG 549 – O8 V
1056	00 57 27.79	-72 09 44.9	7.43	15.33	-0.06	A0 II	
1057	00 59 20.28	-72 14 25.0	4.18	15.34	-0.17	B0 V	
1058	00 59 07.63	-72 10 48.3	0.46	15.35	-0.26	O8: Vn	NMC 16, MPG 500 – O6 V: +neb
1059	00 59 31.47	-72 08 00.0	3.17	15.36	-0.24	B0 V	Binary (SB1)
1060	00 59 04.79	-72 11 02.9	0.64	15.39	-0.15	O8 V	Binary (SB1); NMC 19, MPG 445 – O7.5 V; †
1061	00 57 47.68	-72 17 18.0	9.06	15.39	-0.21	B0 V	2dFS#1263 – O9.5 Ib
1062	01 00 07.25	-72 09 36.9	4.87	15.45	-0.27	B1.5 V (shell)	In-filling in wings of Balmer lines
1063	00 57 45.20	-72 08 06.4	6.49	15.48	-0.09	B5e	MA93#1032
1064	00 58 18.87	-72 18 33.2	8.86	15.50	-0.24	B1.5 III	Binary (SB1)
1065	00 58 40.55	-72 11 06.4	1.96	15.52	0.02	A0 II	NMC 46, MPG 167
1066	00 59 42.71	-72 14 21.9	4.92	15.53	-0.16	B1-2e	KWB346#259
1067	00 58 22.90	-72 17 51.4	8.10	15.53	-0.24	O9 V	

continued on next page

Table A.1. *continued*

Star	$\alpha(2000)$	$\delta(2000)$	r_d	V	$B - V$	Spectral Type	Comments
1068	00 58 31.75	-72 15 49.6	5.97	15.54	-0.15	B0.7 III	2dFS#1321 – B0-5 (III)
1069	00 58 21.20	-72 17 46.8	8.08	15.54	-0.23	B0: + B0.5:	Binary (SB2)
1070	00 59 20.60	-72 09 58.0	1.31	15.54	-0.25	B2 III	MPG 701
1071	00 59 00.96	-72 11 09.2	0.79	15.54	-0.25	O6.5 Vz	NMC 34, MPG 356 – O6.5 V+neb
1072	00 57 39.89	-72 06 01.3	7.82	15.55	-0.26	B0.2 V	2dFS#1247 – B1-5 (II)
1073	00 59 04.57	-72 10 37.7	0.22	15.55	-0.27	B0 V	MPG 439
1074	00 59 11.27	-72 10 01.3	0.65	15.59	-0.21	B0.5 V	MPG 583; str. H II
1075	01 00 11.82	-72 09 51.3	5.18	15.60	-0.25	B1 III	
1076	00 58 14.95	-72 16 36.4	7.26	15.62	-0.18	B1 III	
1077	01 00 17.42	-72 07 38.6	6.23	15.64	-0.29	B2.5 III	
1078	00 58 11.57	-72 14 28.2	5.73	15.64	-0.26	B0.5 III	2dFS#1292; blended in WFI image with 1093
1079	00 59 11.90	-72 10 55.8	0.77	15.64	-0.24	B0 III	NMC 12, MPG 595 – B0 V; †
1080	00 59 18.29	-72 04 21.0	6.15	15.65	-0.28	B0.5 III	
1081	00 58 03.37	-72 16 29.0	7.67	15.65	-0.14	B1 III	
1082	01 00 16.71	-72 14 34.0	6.92	15.65	-0.31	B0 III	
1083	00 59 17.42	-72 13 47.3	3.52	15.66	-0.15	B3 III	
1084	01 00 21.93	-72 08 44.1	6.16	15.66	-0.30	B1.5 III	
1085	00 57 20.52	-72 10 21.1	7.96	15.68	-0.17	B3 III	
1086	00 59 10.45	-72 10 47.0	0.59	15.68	-0.22	O8 V	MPG 561
1087	00 59 07.33	-72 13 21.2	2.95	15.69	-0.18	B2 III	
1088	01 00 14.44	-72 09 00.6	5.53	15.69	-0.35	B2.5 III	
1089	00 58 01.71	-72 17 48.5	8.82	15.73	-0.12	B3e	
1090	00 59 06.58	-72 10 30.5	0.19	15.73	-0.09	B0-3 V	MPG 485; str. H II
1091	01 00 16.65	-72 13 20.1	6.25	15.74	-0.30	B0.5: + B0.5:	Binary (SB2)
1092	00 59 10.83	-72 13 38.3	3.26	15.75	-0.22	B1 V	
1093	00 58 11.42	-72 14 29.2	5.75	15.75	-0.26	B1 V	2dFS#1292; blended in WFI image with 1078
1094	00 59 15.87	-72 11 10.7	1.16	15.76	-0.17	O8 V	MPG 658; KWB346#459; str. H II
1095	00 57 30.32	-72 15 58.4	9.10	15.76	-0.24	B3e	
1096	00 58 42.47	-72 11 13.9	1.87	15.77	-0.11	B0.5 V	MPG 183
1097	00 58 24.42	-72 05 32.5	5.75	15.79	-0.25	B0.5: + early B	Binary (SB2)
1098	00 58 52.19	-72 17 19.2	6.97	15.79	-0.16	B1.5 V	
1099	00 58 01.06	-72 18 29.7	9.43	15.80	0.07	A7 III	
1100	00 59 02.06	-72 11 02.4	0.66	15.80	-0.03	B1: (Herbig?)	NMC 33, MPG 374, KWB346#191; str. H II
1101	00 59 14.98	-72 11 35.2	1.42	15.82	-0.21	B0.5:	Binary (SB1); NMC 1, MPG 644
1102	00 59 36.95	-72 17 02.9	7.09	15.83	-0.15	B2 (shell)	2dFS#1406 – B1-3 (III)
1103	00 58 34.36	-72 09 03.9	2.67	15.32	0.80	F8 I	MPG 125; †
1104	00 57 59.60	-72 09 22.6	5.07	15.90	-0.15	B5 II	
1105	00 59 26.81	-72 11 31.7	2.04	15.91	-0.17	B1-3 V	MPG 757
1106	00 57 45.60	-72 06 42.3	7.08	15.91	0.05	A5 III	
1107	00 59 10.28	-72 10 42.7	0.53	15.91	-0.29	O9.5 V	MPG 557
1108	00 57 07.28	-72 10 50.1	8.98	15.93	-0.24	B2 III	
1109	00 57 57.02	-72 16 06.8	7.69	15.94	-0.21	B1.5 III	
1110	01 00 02.06	-72 10 03.6	4.42	15.95	-0.16	B1-3e	MA93#1178, KWB346#543
1111	00 59 45.44	-72 11 41.6	3.39	15.97	0.07	A5 III	MPG 820
1112	00 57 02.96	-72 07 59.7	9.61	15.98	-0.27	B0 V	2dFS#1188 – B0 (V)
1113	00 57 53.34	-72 14 47.3	6.99	15.98	-0.17	B3 III	
1114	01 00 18.26	-72 07 51.8	6.19	15.98	-0.37	O9 V	
1115	01 00 10.87	-72 07 06.6	6.06	15.99	-0.18	Early Be	
1116	00 58 25.10	-72 19 09.8	9.26	16.00	-0.21	Early B+Early B	Binary (SB2); OGLE104222 (EB)
1117	00 59 54.15	-72 06 47.3	5.25	16.00	-0.25	B2 III	
1118	00 57 38.80	-72 06 55.2	7.43	16.02	-0.06	B2.5e	
1119	00 59 52.37	-72 08 02.7	4.36	16.03	-0.21	B1 V	
1120	00 57 37.52	-72 17 29.8	9.72	16.03	-0.07	B8 II	2dFS#1243 – B8 (II)
1121	00 58 11.12	-72 15 47.1	6.75	16.03	-0.02	A0 II	
1122	00 59 50.10	-72 14 41.1	5.52	16.04	-0.12	B2.5 III	Binary (SB1)
1123	00 57 30.23	-72 13 40.2	7.92	16.04	-0.19	B3e (shell)	
1124	00 58 37.43	-72 13 30.7	3.73	16.04	-0.27	B3 III	
1125	00 58 32.20	-72 14 38.6	4.90	16.05	-0.25	B0 V	
1126	00 59 30.99	-72 09 12.4	2.36	16.07	-0.26	B1 V	MPG 786
1127	00 59 12.39	-72 16 17.6	5.91	16.09	-0.08	B2-3e	
1128	00 59 08.97	-72 11 10.4	0.84	16.11	0.04	O7.5 V((ff))	MPG 529
1129	00 59 32.81	-72 08 04.4	3.19	16.13	-0.17	B1.5 V	
1130	00 59 10.84	-72 17 17.7	6.90	16.14	-0.15	B1-3e	Binary (SB1); MA93#1122,
1131	01 00 17.21	-72 07 44.2	6.17	16.14	-0.24	B3 III	
1132	00 59 42.54	-72 16 07.2	6.41	16.15	-0.22	B1 V	
1133	00 58 07.01	-72 16 24.3	7.44	16.15	-0.19	B1 V	
1134	00 58 44.91	-72 08 26.4	2.48	16.16	-0.02	B0:e	MA93#1097, KWB346#374
1135	00 58 03.36	-72 10 50.4	4.70	16.17	-0.20	B1 V	
1136	00 58 37.89	-72 16 28.8	6.40	16.18	-0.07	B1-3e	
1137	00 59 58.00	-72 16 15.9	7.14	16.18	-0.20	B2 V	
1138	00 57 24.40	-72 15 47.9	9.37	16.20	-0.16	B1-3e	MA93#1004
1139	00 59 14.06	-72 07 52.1	2.65	16.20	-0.02	A2 II	
1140	00 59 17.01	-72 10 55.5	1.09	16.20	-0.22	B0 V	MPG 670
1141	00 57 20.13	-72 11 15.2	8.03	16.21	-0.23	B2 III	

continued on next page

Table A.1. *continued*

Star	$\alpha(2000)$	$\delta(2000)$	r_d	V	$B - V$	Spectral Type	Comments
1142	00 59 29.16	-72 08 39.4	2.58	16.21	-0.18	B1.5 III	
1143	00 59 36.89	-72 14 43.8	4.98	16.22	-0.20	B1.5 V	
1144	00 59 11.66	-72 14 24.7	4.04	16.23	-0.16	O9.5 V	2dFS#1369 – O9 V
1145	00 59 50.32	-72 14 49.0	5.63	16.24	-0.20	B2.5 V	
1146	00 58 09.62	-72 15 27.7	6.57	16.24	-0.09	B1-3e	MA93#1059, KWB346#309
1147	00 57 34.21	-72 12 40.8	7.27	16.25	-0.12	B1-3e	MA93#1016
1148	01 00 01.02	-72 15 25.7	6.62	16.27	-0.13	B1-3e	MA93#1176
1149	00 59 06.82	-72 17 19.6	6.92	16.27	-0.16	B2.5 V	
1150	00 58 27.84	-72 16 08.0	6.37	16.27	-0.19	B1 V	
1151	00 59 54.91	-72 11 04.0	3.91	16.27	-0.14	B1-2e	MPG 860, MA93#1171, KWB346#529
1152	00 57 12.23	-72 13 09.3	9.02	16.28	-0.05	B9 II	
1153	00 57 49.14	-72 13 30.9	6.55	16.29	-0.15	B2 V	
1154	00 57 54.86	-72 07 19.4	6.16	16.29	-0.22	B1.5 V	2dFS#1273 – B0-5 (IV)
1155	00 58 44.28	-72 10 25.8	1.55	16.30	-0.21	B1.5 III	MPG 200
1156	00 59 43.56	-72 04 48.8	6.35	16.30	-0.16	B1-3e	MA93#1161
1157	00 59 26.06	-72 05 57.2	4.75	16.30	-0.09	A0 III-II	
1158	00 58 28.25	-72 11 01.2	2.84	16.32	-0.20	B3 Ve	MPG 87
1159	00 59 04.05	-72 09 46.2	0.64	16.34	-0.26	B1.5 V	MPG 422
1160	00 59 22.48	-72 07 37.1	3.11	16.34	-0.19	B1 V	
1161	00 59 19.78	-72 09 56.5	1.26	16.34	-0.22	B2 V	MPG 694
1162	00 59 44.25	-72 09 07.3	3.31	16.34	-0.09	A0 II	MPG 815
1163	00 59 50.52	-72 10 28.9	3.52	16.35	-0.25	B1 V	MPG 842
1164	00 58 40.14	-72 10 25.0	1.86	16.35	-0.16	B3 V	MPG 163
1165	01 00 22.65	-72 14 05.6	7.02	16.35	-0.32	B1.5 V	
1166	00 59 10.85	-72 18 05.8	7.70	16.36	-0.24	B1-3e	
1167	00 59 39.66	-72 10 57.3	2.75	16.37	-0.22	B1.5 V	MPG 806
1168	00 57 48.10	-72 08 20.0	6.20	16.38	-0.06	B9 II	
1169	00 57 13.64	-72 15 23.0	9.83	16.38	-0.08	B9 II	
1170	00 59 40.75	-72 07 52.2	3.76	16.38	-0.27	B0.5 V	
1171	00 59 41.69	-72 03 47.0	7.21	16.38	0.00	A2 III-II	
1172	00 57 56.61	-72 15 58.8	7.62	16.39	-0.14	B3 V	Binary (SB1)
1173	00 58 20.39	-72 12 54.8	4.20	16.39	-0.22	B1 V	
1174	00 59 41.00	-72 04 34.9	6.47	16.40	-0.11	B1-3e	MA93#1160
1175	00 57 20.27	-72 12 56.1	8.37	16.41	-0.19	B2 V	
1176	00 59 15.90	-72 17 38.7	7.29	16.41	-0.24	B1.5 V	
1177	00 59 51.54	-72 16 20.2	6.93	16.42	-0.11	B1-3e	MA93#1166
1178	00 57 39.47	-72 14 08.5	7.50	16.42	-0.20	B1.5 V	
1179	00 58 06.95	-72 08 58.3	4.63	16.42	-0.23	B1.5 V	
1180	01 00 16.11	-72 16 06.0	7.90	16.43	-0.31	B0.5 V	
1181	00 58 57.14	-72 12 25.0	2.08	16.43	-0.05	B1 V	Binary (SB1); MPG 318
1182	01 00 10.51	-72 14 20.5	6.40	16.43	-0.40	B0.5 V	Binary (SB1)
1183	00 57 29.92	-72 04 59.8	9.04	16.44	-0.19	B2.5 V	
1184	01 00 09.54	-72 12 20.0	5.34	16.44	-0.26	B1-3 V	Asymmetric He lines; OGLE210052 (EB)
1185	00 59 12.90	-72 09 50.1	0.86	16.44	-0.24	B0 V	NGC 57, MPG 621; str. nebular spectrum
1186	00 59 43.67	-72 07 37.6	4.09	16.45	-0.22	B2 V	
1187	00 58 27.46	-72 09 42.8	2.92	16.45	-0.09	B5e	MPG 85
1188	00 59 29.40	-72 07 54.6	3.15	16.46	-0.09	B1-2 V	
1189	00 59 28.97	-72 11 23.4	2.11	16.46	-0.25	B1 V	MPG 772
1190	00 59 52.93	-72 06 31.1	5.38	16.46	-0.05	B1-3e	KWB346#526; †
1191	00 58 29.75	-72 09 06.9	2.96	16.46	-0.20	B1.5 V	Binary (SB1); MPG 99
1192	00 58 12.29	-72 17 43.7	8.34	16.46	-0.18	B2 V	Binary (SB1)
1193	00 57 45.09	-72 15 03.4	7.65	16.47	-0.09	B1-2e	MA93#1031
1194	00 59 04.61	-72 12 19.5	1.91	16.47	-0.12	B3e	MPG 431, KWB346#807
1195	00 59 18.85	-72 13 51.8	3.62	16.48	-0.21	B1.5 V	
1196	00 59 12.61	-72 17 24.4	7.02	16.48	-0.18	B1 V	Binary (SB1)
1197	00 59 36.37	-72 12 48.2	3.42	16.48	-0.21	B1.5 V	MPG 800
1198	00 59 38.60	-72 14 01.7	4.46	16.49	-0.22	B1.5 V	2dFS#1407 – B0-5 (IV)
1199	00 58 53.07	-72 10 03.2	0.94	16.49	-0.21	B0 V	MPG 279, KWB346#751
1200	00 57 53.09	-72 14 21.7	6.74	16.51	-0.19	B1 V	
1201	00 58 12.35	-72 10 12.2	4.00	16.51	-0.17	B2.5 V	MPG 2
1202	00 57 30.78	-72 07 44.9	7.65	16.51	-0.10	A0 II	
1203	00 57 09.73	-72 10 33.1	8.78	16.52	-0.17	B2-3e (shell)	
1204	00 59 31.81	-72 12 13.8	2.77	16.53	0.06	A3 III	MPG 788
1205	00 59 59.94	-72 17 07.4	7.94	16.55	-0.16	B2.5 V	
1206	00 58 21.44	-72 12 28.1	3.88	16.55	-0.17	B2.5 V	MPG 46
1207	00 57 57.19	-72 12 37.0	5.60	16.56	-0.17	B3 V	
1208	00 57 38.29	-72 12 52.2	7.04	16.56	-0.21	B2.5 V	
1209	00 59 43.43	-72 15 39.6	6.04	16.57	-0.10	B3 V	Binary (SB1)
1210	00 59 30.31	-72 16 57.1	6.83	16.57	-0.14	B3e (shell)	MA93#1150
1211	00 59 00.08	-72 05 52.6	4.55	16.57	-0.24	B1.5 V	
1212	00 59 04.42	-72 07 06.5	3.30	16.58	-0.16	B3e	KWB346#814
1213	00 57 57.53	-72 14 59.2	6.87	16.58	-0.05	B1-3e	MA93#1047, KWB346#575
1214	00 59 09.67	-72 05 27.8	4.96	16.59	-0.11	B1-3e	MA93#1120, KWB346#856
1215	00 57 36.72	-72 15 12.1	8.25	16.60	-0.16	B3 III	

continued on next page

Table A.1. *continued*

Star	$\alpha(2000)$	$\delta(2000)$	r_d	V	$B - V$	Spectral Type	Comments
1216	00 59 14.67	-72 08 26.0	2.13	16.61	-0.26	B1.5 V	
1217	00 59 44.79	-72 15 26.7	5.90	16.62	-0.18	B2.5 V	
1218	00 59 41.81	-72 16 05.1	6.35	16.62	-0.14	B2.5 V	
1219	01 00 03.31	-72 09 39.1	4.57	16.62	-0.28	B1.5 V	
1220	00 58 44.61	-72 08 43.3	2.27	16.63	-0.24	B1.5 V	
1221	00 59 07.34	-72 13 12.8	2.81	16.63	-0.17	B0.5 V	
1222	00 59 26.95	-72 13 59.3	3.97	16.64	-0.26	B1 V	
1223	01 00 19.50	-72 12 58.2	6.29	16.64	-0.32	B1 V	
1224	00 57 49.04	-72 05 44.2	7.43	16.64	-0.09	B1-2e	
1225	00 58 47.83	-72 16 06.6	5.84	16.65	-0.17	B3 V	
1226	01 00 11.92	-72 14 33.9	6.62	16.65	-0.22	B1.5 V	
1227	00 57 16.74	-72 12 38.9	8.54	16.67	-0.19	B3 V	
1228	00 58 22.55	-72 18 58.5	9.15	16.67	-0.05	B9 II	
1229	00 59 36.11	-72 14 32.1	4.78	16.67	-0.20	B1.5 V	
1230	00 58 18.60	-72 11 41.0	3.74	16.67	-0.27	B0.5 V	MPG 33
1231	00 59 11.79	-72 12 36.1	2.26	16.67	-0.09	B8 II	MPG 588
1232	00 58 57.30	-72 10 28.7	0.55	16.67	-0.25	B1 V	MPG 323
1233	00 58 31.45	-72 12 24.6	3.22	16.68	-0.25	B0.2 V	MPG 111
1234	00 58 58.98	-72 13 18.0	2.92	16.68	-0.13	B2.5 V	
1235	00 58 00.11	-72 12 45.7	5.46	16.69	-0.17	B3 V	
1236	00 59 10.02	-72 11 30.3	1.17	16.69	-0.22	B1 V	MPG 550
1237	00 58 17.19	-72 02 34.4	8.63	16.69	-0.17	B3e	
1238	01 00 14.48	-72 12 06.7	5.62	16.69	-0.30	B2.5 V	
1239	00 58 15.57	-72 16 45.6	7.37	16.70	-0.17	B2 V	
1240	00 58 01.84	-72 14 47.3	6.49	16.70	-0.18	B3 V	
1241	00 59 30.45	-72 11 35.7	2.31	16.71	-0.10	B1 V	Binary (SB1); MPG 781
1242	01 00 13.23	-72 07 18.5	6.11	16.71	-0.24	B2 V	
1243	00 58 58.00	-72 06 25.1	4.02	16.72	-0.15	B3 V	
1244	00 59 21.70	-72 11 10.9	1.53	16.73	-0.21	B2.5 V	MPG 710
1245	00 57 56.91	-72 14 12.0	6.41	16.73	-0.19	B1.5 V	
1246	00 59 54.80	-72 15 26.3	6.33	16.74	-0.18	B3 V	Binary (SB1); OGLE207517 (EB)
1247	00 59 08.87	-72 10 36.4	0.39	16.74	-0.24	B1.5 V	MPG 527

†: Further notes on individual stars:

1001: Walborn (1978); Walborn & Blades (1986): O4 III(n)(f)

1002: Humphreys (1983): B3 I; Lennon (1997): B1.5 Ia

1003: Humphreys (1983): B3 I

1007: Massey et al. (1995): B1 III

1008: Walborn & Blades (1986): O3 III (f*); Niemela et al. (1986): O3 III(f); Walborn et al. (2000): ON3 III(f*); Walborn et al. (2002): O2 III(f*)

1010: Walborn & Blades (1986); Niemela et al. (1986): O5-6 V; Massey et al. (2009, but noted as triple system): O5.5 III((f))

1011: Garmany et al. (1987): O9 III; Walborn et al. (1995): O9 III

1012: Niemela et al. (1986): O5-6: V; Walborn et al. (2000): O4-5 V((f))

1018: Garmany et al. (1987): B0n

1019: Classification adopted from Walborn et al. (2000), also classified as O7 If by Garmany et al. (1987).

1030: Heydari-Malayeri & Selier (2010): O5 V + OB

1052: Heydari-Malayeri & Selier (2010): O9.5 V

1060: Heydari-Malayeri & Selier (2010): O8 V

1079: Heydari-Malayeri & Selier (2010): B0-0.5 V

1103: EIS photometry has a non-physical (negative) colour, adopted photometry is from Massey et al. (1989).

1190: MA93#1169 is a blend of this and another star.

Table A.2. Atmospheric parameters (T_{eff} , $\log g$) and projected rotational velocities ($v_e \sin i$), luminosities, current masses and ages for the NGC 346 sample. The fourth column indicates the method used to estimate the effective temperature, viz. H08: taken from Hunter et al. (2008b); M06: taken from Mokiem et al. (2006); A: adopted from effective temperature scales of Trundle et al. (2007); I: interpolated from these temperature scales; E: extrapolated from these temperature scales; M: luminosity class V assumed; Si: silicon ionization balance; He: He I line at 4026Å; He+: He II lines at 4541 and 4686Å; L: literature. Two methods were used to estimate the $v_e \sin i$: profile fitting (PF) and Fourier transform (FT). Targets marked with an asterisk appear to be overluminous for an assumed luminosity class V and their estimates should be treated with caution. SB1 in the final column indicates that significant radial velocity variables were detected while the double-lined spectroscopic binaries are designated as SB2 (and one tripled-lined system as SB3). Many of the Be-type stars from the FSMS were classified by (Evans et al. 2006) as ‘(Be-Fe)’ to indicate Fe II emission. This spectral qualifier has not been used further elsewhere (including for the Survey spectra here) but for completeness cf. the published types, these suffixes are included below.

Star	Spectral Type	T_{eff} (K)	Method	$\log g$ (dex)	$v_e \sin i$		r ($'$)	$\log L$ (L_{\odot})	Mass (M_{\odot})	Age (Myr)	Comment
					PF (km s^{-1})	FT					
0001	O7 Iaf+	34100	M06	3.35	74	76	2.13	5.97	55.6	2.9	SB1
0002	A2: Iab	–	–	–	–	–	5.55	–	–	–	
0003	G0:	–	–	–	–	–	3.36	–	–	–	
0004*	Be (B1:)	27300	AM	3.00	266	258	7.22	5.16	22.4	6.6	
0005	A0 II	–	–	–	–	–	8.49	–	–	–	
0006	F2:	–	–	–	–	–	5.69	–	–	–	
0007	O4 V((f+))	42800	M06	3.95	120	113	0.56	5.54	38.4	2.4	SB1
0008*	B1e	27300	AM	3.05	299	295	5.74	4.96	17.6	7.8	
0009*	B0e	32000	AM	3.25	199	187	3.74	5.07	19.8	7.2	
0010	O7 IIIIn((f))	35900	M06	3.54	313	339	6.88	5.21	25.8	4.2	
0011	B9 II	–	–	–	–	–	9.17	–	–	–	
0012	B1 Ib	24200	H08	3.20	≤ 40	≤ 40	4.82	4.77	14.6	11.1	
0013*	B1:	27300	AM	3.75	120	121	2.34	4.89	17.4	8.5	SB2
0014	A0 II	–	–	–	–	–	4.99	–	–	–	
0015	B1 V	27300	A	3.85	–	–	8.47	4.79	15.8	9.2	SB2
0016	B0.5 Vn	29650	A	3.95	181	163	6.04	4.87	17.8	7.6	SB2
0017*	Be (B1)	27300	AM	3.25	231	226	7.54	4.77	15.8	9.1	SB1
0018	O9.5 IIIe	32700	M06	3.33	138	130	2.93	4.93	19.2	6.0	
0019	A0 II	–	–	–	–	–	2.37	–	–	–	
0020	B1 V+early-B	27300	A	3.75	–	–	6.41	4.68	14.6	10.1	SB2
0021	B1 III	25150	H08	3.50	≤ 40	≤ 40	4.58	4.60	15.0	10.0	
0022	O9 V	36800	M06	4.20	55	58	1.32	5.02	22.6	4.1	
0023*	B0.2: (Be-Fe)	30800	AM	3.75	65	57	1.94	4.81	18.8	5.8	
0024*	B2: shell(Be-Fe)	24950	AM	3.10	190	197	2.67	5.00	17.2	8.4	
0025	O9 V	36200	M06	4.07	138	138	3.73	4.99	21.8	4.3	SB1
0026	B0 IV (Nstr)	31000	H08	3.70	75	68	3.87	4.79	17.0	7.3	
0027	B0.5 V	31000	H08	4.05	220	241	3.12	4.78	17.2	7.1	
0028	OC6 Vz	42900	M06	3.97	≤ 40	≤ 40	2.56	5.16	30.4	1.2	
0029	B0 V	32150	H08	4.10	≤ 40	≤ 40	1.76	4.82	17.6	6.7	SB1
0030	B0 V	32000	A	4.15	183	181	4.27	4.81	17.8	6.6	SB2
0031	O8 Vz	39500	M06	3.99	≤ 40	≤ 40	7.01	5.06	25.2	2.9	
0032	B0.5 V	29000	H08	4.40	125	118	5.83	4.68	15.2	8.8	SB1
0033	O8 V	39900	M06	4.44	188	170	0.71	5.05	25.8	2.4	
0034	O8.5 V	37400	I	–	206	190	0.44	4.97	22.8	3.6	SB1
0035	B1 V	27300	A	3.75	145	–	5.84	4.60	14.0	10.3	SB2
0036	B0.5 V(Be-Fe)	29650	A	3.45	287	276	2.15	4.68	15.8	8.0	
0037	B3 III	18800	H08	3.20	≤ 40	≤ 40	4.07	4.20	8.8	24.4	
0038	B1 V	27300	A	4.00	158	160	5.34	4.57	12.8	13.1	
0039	B0.7 V	25800	H08	3.60	≤ 40	≤ 40	8.60	4.51	12.6	12.6	SB1
0040	B0.2 V	30600	H08	4.00	≤ 40	≤ 40	3.46	4.67	15.4	8.0	SB1
0041	B2 (Be-Fe)	24950	A	3.85	144	144	8.42	4.46	12.2	13.4	
0042	A7 II	–	–	–	–	–	8.39	–	–	–	
0043	B0 V	33000	H08	4.25	≤ 40	≤ 40	4.02	4.71	17.0	6.2	
0044	B1 II	23000	H08	3.50	≤ 40	≤ 40	3.25	4.33	10.6	17.2	
0045	B0.5 Vne	29650	A	3.75	181	173	3.89	4.56	14.4	8.5	
0046	O7 Vn	39700	M06	4.17	340	378	3.80	4.90	25.0	1.0	
0047	B2.5 III	19850	H08	3.25	63	55	9.35	4.15	9.0	23.7	
0048	Be (B3 shell)	21500	EM	3.15	≤ 40	≤ 40	2.55	4.22	9.6	20.7	
0049	B8 II	13000	H08	2.70	72	64	7.70	3.70	–	–	

continued on next page

Table A.2. *continued*

Star	Spectral Type	T _{eff} (K)	Method	log <i>g</i> (dex)	<i>v</i> _e sin <i>i</i>		<i>r</i> (′)	log L (L _⊙)	Mass (M _⊙)	Age (Myr)	Comment
					PF (km s ⁻¹)	FT					
0050	O8 Vn	37200	M06	4.16	357	340	1.48	4.80	21.6	2.5	
0051	O7 Vz	41600	M06	4.33	≤ 40	≤ 40	0.37	4.93	26.4	0.0	
0052	B1.5 V	26100	A	3.85	≤ 40	≤ 40	6.93	4.39	11.8	13.1	SB2
0053	B0.5 V	29500	H08	3.75	170	174	7.60	4.51	14.0	8.7	SB1
0054	B1 V	29000	H08	4.30	≤ 40	≤ 40	2.88	4.47	13.2	9.8	
0055	B0.5 V	29500	H08	4.00	130	137	3.20	4.49	13.8	8.9	
0056	B0 V	31000	H08	3.80	≤ 40	≤ 40	1.06	4.55	14.6	7.8	
0057	B2.5 III	19850	H08	3.35	73	80	5.38	4.08	8.6	25.6	
0058	B0.5 V	29500	H08	4.25	180	192	3.40	4.47	13.6	8.7	SB1
0059	A5 II	–	–	–	–	–	5.33	–	–	–	
0060	B0.5e (shell)	29650	AM	3.40	311	286	4.75	4.46	14.0	8.1	
0061	B1-2 (Be-Fe)	26100	IM	3.55	336	329	5.68	4.32	11.8	11.9	
0062	B0.2 V	29750	H08	4.00	≤ 40	≤ 40	6.61	4.45	13.4	9.0	
0063	A0 II	–	–	–	–	–	5.69	–	–	–	
0064	B1-2 (Be-Fe)	26100	IM	3.85	108	120	5.44	4.31	11.4	13.3	
0065	B3 (Be-Fe)	21500	EM	3.25	222	238	1.88	4.12	9.4	20.9	
0066	O9.5 V	35600	M06	4.25	129	116	1.86	4.65	18.4	3.2	
0067	B1-2 (Be-Fe)	26100	IM	3.35	351	339	6.19	4.30	11.8	11.9	
0068	B0 V (Be-Fe)	32000	A	3.85	378	384	5.60	4.51	15.8	5.4	
0069	B1-2 (Be-Fe)	26100	IM	3.75	186	170	9.43	4.28	11.2	13.2	
0070	B0.5 V	30500	H08	4.15	109	102	3.56	4.43	13.8	13.8	
0071	A0 II	–	–	–	–	–	7.85	–	–	–	
0072	B1-2 (Be-Fe)	26100	IM	3.85	102	95	3.32	4.26	11.0	13.6	
0073	B1-2 (Be-Fe)	26100	IM	3.80	190	179	7.21	4.26	11.2	13.2	
0074	B3 III	16300	H08	3.20	52	62	8.30	3.79	6.6	40.8	
0075	B1 V	27700	H08	4.30	≤ 40	≤ 40	4.68	4.31	11.8	11.6	SB1
0076	B2 (Be-Fe)	24950	AM	3.40	237	247	1.88	4.21	10.6	14.6	
0077	O9 V	36500	M06	3.99	177	169	1.31	4.62	19.0	1.2	
0078	B2 III	21200	A	3.60	154	163	5.43	4.05	8.8	23.0	
0079	B0.5 Vn	29500	H08	4.20	293	308	0.34	4.37	13.4	8.0	
0080	B1 V	27300	H08	4.25	216	203	1.14	4.28	11.6	11.4	
0081	B2 III _n	21200	H08	3.50	255	260	5.61	4.03	8.8	22.4	
0082	B2 III	21200	H08	3.70	168	166	5.78	4.03	8.8	23.0	SB1
0083	B1 V	27300	H08	4.05	207	200	1.83	4.28	11.6	11.4	
0084	B1 V	27300	H08	4.25	105	95	5.88	4.27	11.4	11.9	
0085	B2 III	21200	A	3.55	≤ 40	≤ 40	6.63	4.03	8.6	24.6	SB2
0086	B0.2 V	30800	A	4.25	188	190	5.09	4.54	17.2	2.4	
0091	B1e	27300	AM	3.85	49	52	8.68	4.25	11.4	12.1	SB1
0092	B1 Vn	27300	H08	3.95	234	240	4.14	4.24	11.6	11.1	
0093	B0 V	34400	M06	4.40	187	196	0.74	4.50	16.6	2.6	
0094	B0.7 V	28500	H08	4.00	≤ 40	≤ 40	5.28	4.28	11.8	10.5	
0095	B1-2 (Be-Fe)	26100	IM	3.90	227	236	8.43	4.18	10.8	13.1	
0096	B1-2 (Be-Fe)	26100	IM	3.35	343	337	8.38	4.18	11.0	12.1	
0097	O9 V	37500	M06	4.49	≤ 40	≤ 40	0.86	4.58	19.2	0.0	
0098	B1.5 V	26100	H08	4.05	56	60	2.70	4.16	10.4	14.2	
0099	B3 III	18000	H08	3.40	94	98	8.63	3.79	7.0	36.8	
0100	B1.5 V	26100	H08	4.30	183	174	6.89	4.16	10.6	13.6	
0101	B1 V	27300	H08	4.25	≤ 40	≤ 40	4.96	4.18	11.0	12.4	
0102	B3 III	17700	H08	3.70	≤ 40	≤ 40	5.34	3.75	6.8	40.9	
0103	B0.5 V	29500	H08	4.00	≤ 40	≤ 40	7.54	4.26	12.2	8.8	
0104	B0 V	32500	H08	4.35	≤ 40	≤ 40	1.19	4.37	14.4	4.5	SB1
0105	B2 III	21200	A	3.50	193	208	3.50	3.92	8.2	24.8	SB1
0106	B1 V	27500	H08	4.20	142	135	7.49	4.17	11.0	11.4	SB1
0107	O9.5 V	35900	M06	4.23	55	60	0.45	4.48	17.4	0.0	
0108	B1.5 V	26100	H08	3.95	167	171	4.59	4.11	10.4	13.7	
0109	B1.5 V	26100	H08	4.25	123	119	6.03	4.11	10.4	13.7	
0110	B1-2 (Be-Fe)	26100	I	3.95	243	232	5.91	4.11	10.4	13.7	SB1

continued on next page

Table A.2. *continued*

Star	Spectral Type	T _{eff} (K)	Method	log <i>g</i> (dex)	<i>v</i> _e sin <i>i</i>		<i>r</i> (′)	log L (L _⊙)	Mass (M _⊙)	Age (Myr)	Comment
					PF (km s ⁻¹)	FT					
0111	B0.5 V	28000	He+	4.10	57	49	0.49	4.18	10.8	10.7	
0112	O9.5 V	34400	M06	4.15	143	141	1.76	4.41	16.0	0.8	
0113	B0.5 V	29650	A	4.00	122	132	4.10	4.22	12.2	7.6	
0114	B1 Vn	27300	H08	3.90	287	291	5.16	4.13	11.2	10.4	
0115	B0.2 V	30800	A	4.05	133	120	0.11	4.25	13.0	5.7	
0116	B1 V	28250	H08	4.10	≤ 40	≤ 40	6.26	4.15	11.2	10.4	
1001	O4-6 If +?	–	–	–	180	156	0.00	–	–	–	SB2
1002	B1.5 Ia	20650	A	2.55	67	51	6.39	5.25	–	–	SB1
1003	B3 Iab	15700	Si	2.15	43	≤ 40	6.79	4.91	–	–	
1004	A2 Ib	–	–	–	–	–	9.13	–	–	–	
1005	A2 Ib	–	–	–	–	–	9.33	–	–	–	
1006	A2 Ib	–	–	–	–	–	4.7	–	–	–	
1007	B1 Ia	21500	Si	2.65	79	66	2.97	5.03	17.6	9.1	SB1
1008	O2 III(f ^a st)	51700	L	4.00	110	130	0.29	6.00	57.4	1.9	
1009*	B1e	27300	AM	3.25	75	81	4.22	5.20	22.8	6.6	
1010	O6: V-III((f))	42970	A	–	–	–	0.40	5.70	45.0	2.3	SB3
1011	O9 III	33800	Si	3.75	77	86	5.06	5.38	28.2	4.5	SB1
1012	O6: V((f))	39300	L	3.75	60	58	0.23	5.40	32.2	3.1	SB1
1013*	0.5e	29650	AM	3.65	245	259	0.50	5.02	19.8	6.8	
1014	B3 Ib + mid A?	15500	A	2.25	≤ 40	≤ 40	4.76	4.32	–	–	SB2?
1015	O7 V	40730	A	–	119	135	0.21	5.33	30.8	2.9	
1016	B8 Ib	12500	He	2.45	44	≤ 40	2.45	4.08	–	–	
1017	O9 V	36265	A	–	260	239	5.95	5.19	25.6	4.2	SB2
1018*	B0ne (shell)	32000	AM	3.50	290	313	9.73	5.03	21.0	5.9	
1019	O6.5f?p	37500	L	3.75	≤ 40	46	4.63	5.22	26.6	3.9	
1020	B1 III	23950	A	3.50	90	81	6.19	4.71	14.0	11.8	SB1
1021	B2 II	20075	AI	3.25	152	143	3.60	4.49	11.2	17.2	
1022	B2 II	20075	AI	3.00	190	187	8.87	4.49	11.2	17.2	
1023	B0 V	31750	He+	3.90	175	178	3.40	4.95	19.4	6.3	SB1
1024	B	–	–	–	–	–	1.99	–	–	–	
1025	O7 V	40730	A	–	218	257	0.97	5.24	29.6	2.7	
1026	O6.5 V((f))	41850	A	–	≤ 40	46	0.94	5.26	30.8	2.4	
1027*	B0-3e	26100	AM	3.75	246	258	9.26	4.71	15.0	9.9	
1028	B2.5 III	22000	Si	3.45	≤ 40	≤ 40	7.75	4.29	10.2	18.8	
1029	B2.5 III	19850	A	3.25	53	55	6.48	4.38	10.0	19.9	
1030	OC5 V	45200	A	–	≤ 40	–	1.15	5.27	35.6	0.4	
1031*	B2-3e	24290	EM	3.30	215	233	2.88	4.55	13.0	12.4	
1032*	B0.5:e	29650	AM	3.55	367	345	8.51	4.73	16.0	7.6	
1033	B0 V	33500	He+	4.40	312	310	0.36	4.87	19.4	5.4	
1034	O9.5-B0 V	35000	I	4.35	378	375	0.79	4.92	21.0	4.6	
1035	O7.5 V((f))	39615	I	–	82	98	0.44	5.06	25.4	2.7	
1036	B2.5 III-II	19850	A	3.25	50	57	4.39	4.31	9.8	20.7	
1037	B0 III	27700	Si	3.75	83	81	6.51	4.63	14.2	10.0	
1038	B0: e	32000	AM	–	380	372	6.90	4.80	18.2	6.2	
1039	O9.5 V	35150	A	–	149	158	0.37	4.91	20.4	4.8	SB1
1040	Early-B+Early-B	–	–	–	–	–	8.69	–	–	–	SB2
1041	B2 III-II	22500	Si	3.35	≤ 40	≤ 40	8.29	4.43	11.2	16.7	
1042	B1-2e	26100	IM	3.55	266	260	1.86	4.55	13.4	11.1	
1043	B0 V	32000	He+	4.30	147	135	2.82	4.76	17.0	6.7	
1044	B1 III	23950	A	3.75	132	115	8.33	4.46	12.0	14.3	
1045	O9 V	36265	A	–	83	87	0.22	4.90	21.0	4.2	SB1
1046	B0.5 V	29650	A	3.90	281	270	6.92	4.65	15.4	8.0	
1047	A5 III	–	–	–	–	–	7.04	–	–	–	
1048	O9 V	36265	A	–	124	136	0.62	4.88	20.8	4.1	
1049	B0 V	31000	He+	4.25	293	282	0.49	4.74	16.8	7.0	SB2
1050	B1.5 II	24100	Si	3.45	≤ 40	≤ 40	7.02	4.44	11.6	14.6	
1051	O9 V	36265	A	–	≤ 40	≤ 40	5.78	4.88	20.6	4.2	

continued on next page

Table A.2. *continued*

Star	Spectral Type	T _{eff} (K)	Method	log <i>g</i> (dex)	<i>v</i> _e sin <i>i</i>		<i>r</i> (′)	log L (L _⊙)	Mass (M _⊙)	Age (Myr)	Comment
					PF (km s ⁻¹)	FT					
1052	B0 V	34000	He+	4.40	108	120	0.30	4.78	18.2	5.4	
1053	B0.5 III	27500	Si	3.60	≤ 40	≤ 40	6.44	4.50	12.8	11.8	
1054	B1 III	23950	A	3.45	222	234	4.85	4.40	11.6	14.4	SB1
1055	O9.5 V	35150	A	–	53	72	0.70	4.80	19.2	4.7	
1056	A0 II	–	–	–	–	–	7.43	–	–	–	
1057	B0 V	33000	He+	4.10	105	128	4.18	4.72	17.2	6.0	
1058	O8 Vn	38500	A	–	290	316	0.46	4.90	23.6	2.2	
1059	B0 V	30000	He+	4.05	58	62	3.17	4.62	16.2	5.9	SB1
1060	O8 V	38500	A	–	141	148	0.64	4.88	22.8	2.3	SB1
1061	B0 V	31750	He+	4.05	139	132	9.06	4.65	16.0	6.9	
1062	B1.5 V (shell)	26100	A	3.95	114	129	4.87	4.42	12.2	12.4	
1063	B5e	–	–	–	165	164	6.49	–	–	–	
1064	B1.5 III	22550	A	3.60	146	137	8.86	4.26	10.2	18.3	SB1
1065	A0 II	–	–	–	–	–	1.96	–	–	–	
1066	B1-2e	26100	IM	3.65	226	222	4.92	4.39	12.2	12.1	
1067	O9 V	36265	A	–	56	66	8.10	4.76	19.6	3.5	
1068	B0.7 III	25500	He+	3.85	52	60	5.97	4.35	11.4	14.2	
1069	B0: + B0.5:	–	–	–	–	–	8.08	–	–	–	SB2
1070	B2 III	21200	A	3.40	≤ 40	≤ 40	1.31	4.18	9.4	22.1	
1071	O6.5 Vz	38200	A	–	≤ 40	≤ 40	0.79	4.92	26.2	0.0	
1072	B0.2 V	31750	He+	4.35	163	166	7.82	4.59	15.6	6.8	
1073	B0 V	31750	He+	4.40	297	318	0.22	4.59	16.0	6.2	
1074	B0.5 V	29000	He+	4.35	281	253	0.65	4.47	13.6	8.9	
1075	B1 III	23950	A	3.50	104	97	5.18	4.28	10.6	16.3	
1076	B1 III	26500	Si	3.90	65	69	7.26	4.36	11.8	12.7	
1077	B2.5 III	19850	A	3.55	221	230	6.23	4.08	8.8	24.0	
1078	B0.5 III	27500	He+	3.80	105	104	5.73	4.40	12.4	11.2	
1079	B0 III	31000	He+	4.00	≤ 40	≤ 40	0.77	4.50	14.2	7.7	
1080	B0.5 III	27800	Si	3.90	≤ 40	≤ 40	6.15	4.40	12.4	11.3	
1081	B1 III	26400	Si	3.75	≤ 40	≤ 40	7.67	4.35	11.5	13.1	
1082	B0 III	29000	Si	3.85	≤ 40	≤ 40	6.92	4.44	13.0	9.8	
1083	B3 III	16500	Si	3.15	≤ 40	≤ 40	3.52	3.88	7.0	38.5	
1084	B1.5 III	22550	A	3.70	162	164	6.16	4.20	10.2	18.9	
1085	B3 III	18450	A	3.20	205	183	7.96	3.98	8.0	29.1	
1086	O8 V	38500	A	–	163	171	0.59	4.77	22.0	0.8	
1087	B2 III	21200	A	3.50	141	131	2.95	4.12	9.2	22.2	
1088	B2.5 III	19850	A	3.30	187	184	5.53	4.06	8.6	24.7	
1089	B3e	21500	EM	3.65	237	254	8.82	4.12	9.4	20.3	
1090	B0-3 V	26100	IM	3.95	319	332	0.19	4.31	11.8	12.0	
1091	B0.5: + B0.5:	–	–	–	–	–	6.25	–	–	–	SB2
1092	B1 V	27000	He+	4.10	175	170	3.26	4.33	11.8	11.8	
1093	B1 V	26000	He+	4.00	≤ 40	≤ 40	5.75	4.28	11.0	14.1	
1094	O8 V	38500	A	–	124	121	1.16	4.74	21.6	0.4	
1095	B3e	21500	EM	3.75	241	244	9.10	4.12	9.4	20.3	
1096	B0.5 V	30000	He+	4.40	250	281	1.87	4.43	13.8	7.7	
1097	B0.5: + early B	26100	A	3.85	254	272	6.97	4.28	11.4	12.5	
1099	A7 III	–	–	–	–	–	9.43	–	–	–	
1100	B1: (Herbig?)	27300	AM	3.90	173	195	0.66	4.32	12.0	11.3	
1101	B0.5:	29650	AM	4.25	301	311	1.42	4.40	13.6	7.9	SB1
1102	B2 (shell)	24950	AM	3.50	258	264	7.09	4.22	10.8	14.4	
1103	F8 I	–	–	–	–	–	2.67	–	–	–	
1104	B5 II	14500	He	2.85	63	68	5.07	3.65	6.0	52.4	
1105	B1-3 V	24950	I	3.65	281	286	2.04	4.19	10.6	14.4	
1106	A5 III	–	–	–	–	–	7.08	–	–	–	
1107	O9.5 V	34500	He+	4.10	71	79	0.53	4.55	16.8	3.6	
1108	B2 III	21200	A	3.80	99	109	8.98	4.03	8.6	23.8	
1109	B1.5 III	24000	Si	3.60	≤ 40	≤ 40	7.69	4.14	9.8	18.0	

continued on next page

Table A.2. *continued*

Star	Spectral Type	T _{eff} (K)	Method	log <i>g</i> (dex)	<i>v</i> _e sin <i>i</i>		<i>r</i> (′)	log L (L _⊙)	Mass (M _⊙)	Age (Myr)	Comment
					PF (km s ⁻¹)	FT					
1110	B1-3e	24950	IM	3.75	255	240	4.42	4.18	10.6	14.8	
1111	A5 III	–	–	–	–	–	3.39	–	–	–	
1112	B0 V	32100	Si	4.20	69	76	9.61	4.43	14.6	5.8	
1113	B3 III	18450	A	3.30	50	50	6.99	3.87	7.4	33.1	
1114	O9 V	36265	A	–	250	232	6.19	4.58	18.8	0.4	
1115	Early-Be	–	–	–	269	252	6.06	–	–	–	SB2
1116	Early-B+Early-B	–	–	–	–	–	9.26	–	–	–	SB2
1117	B2 III	21200	A	3.70	106	130	5.25	4.00	8.6	23.8	
1118	B2.5e	23900	EM	3.60	210	194	7.43	4.10	9.8	17.	
1119	B1 V	23000	Si	3.60	≤ 40	≤ 40	4.36	4.05	9.0	208	
1120	B8 II	12500	He	3.05	54	70	9.72	3.45	–	–	
1121	A0 II	–	–	–	–	–	6.75	–	–	–	
1122	B2.5 III	19850	A	3.60	125	163	5.52	3.92	8.0	27.9	SB1
1123	B3e (shell)	21500	E	3.35	275	284	7.92	4.00	8.8	21.8	
1124	B3 III	18450	A	3.70	111	126	3.73	3.84	7.4	33.0	
1125	B0 V	33000	He+	4.40	≤ 40	≤ 40	4.90	4.44	15.0	4.6	
1126	B1 V	27300	A	4.20	260	258	2.36	4.21	11.4	10.9	
1127	B2-3e	23900	EM	3.55	223	224	2.36	4.07	9.6	17.3	
1128	O7.5 V((f))	39615	I	–	56	68	0.84	4.63	21.6	0.0	
1129	B1.5 V	26100	A	3.95	176	168	2.36	4.15	10.6	13.6	
1130	B1-3e	24950	IM	4.00	310	309	2.36	4.10	10.2	14.5	SB1
1131	B3 III	18450	A	3.55	≤ 40	≤ 40	6.17	3.80	7.0	36.7	
1132	B1 V	27300	A	4.15	205	225	6.41	4.18	11.2	11.2	
1133	B1 V	27300	A	4.00	≤ 40	≤ 40	7.44	4.18	11.0	12.4	
1134	B0:e	32000	AM	3.95	519	505	2.48	4.36	15.4	4.2	
1135	B1 Vn	27300	A	4.40	301	319	4.70	4.17	11.4	10.3	
1136	B1-3e	24950	IM	3.85	205	225	6.40	4.09	10.0	15.4	
1137	B2 V	24950	A	4.00	108	99	7.14	4.09	9.8	16.3	
1138	B1-3e	24950	IM	3.60	228	208	9.37	4.08	10.0	15.5	
1139	A2 II	–	–	–	–	–	2.65	–	–	–	
1140	B0 V	33250	He+	4.15	159	164	1.09	4.39	15.2	2.8	
1141	B2 III	21200	A	3.75	≤ 40	≤ 40	8.03	3.91	8.0	26.7	
1142	B1.5 III	22550	A	3.70	≤ 40	≤ 40	2.58	3.97	8.6	22.5	
1143	B1.5 V	26100	A	4.50	289	281	4.98	4.11	10.6	12.7	
1144	O9.5 V	35150	A	–	≤ 40	43	4.04	4.44	16.6	0.3	
1145	B2.5 V	23900	E	4.15	102	110	5.63	4.01	9.2	18.7	
1146	B1-3e	24950	IM	3.95	261	271	6.57	4.06	10.0	15.1	
1147	B1-3e	24950	IM	4.05	259	238	7.27	4.06	10.0	15.0	
1148	B1-3e	24950	IM	4.25	221	240	6.62	4.05	9.8	15.3	
1149	B2.5 V	23900	E	3.90	145	142	6.92	4.01	9.2	18.5	
1150	B1 V	26500	A	4.10	76	77	6.37	4.10	10.4	13.4	
1151	B1-2e	26100	IM	3.65	295	301	3.91	4.09	10.6	12.4	
1152	B9 II	–	–	–	–	–	9.02	–	–	–	
1153	B2 V	24950	A	4.30	62	60	6.55	4.04	9.6	16.7	
1154	B1.5 Vn	26100	A	4.10	226	239	6.16	4.08	10.4	13.4	
1155	B1.5 III	22550	A	3.60	111	120	1.55	3.94	8.6	22.2	
1156	B1-3e	24950	IM	3.75	313	308	6.35	4.04	10.0	14.6	
1157	A0 III-II	–	–	–	–	–	4.75	–	–	–	
1158	B3 Ve	21500	E	3.75	226	239	2.84	3.88	8.2	24.0	
1159	B1.5 V	26100	A	4.30	200	198	0.64	4.06	10.2	13.4	
1160	B1 V	27300	A	3.95	315	340	3.11	4.10	11.2	9.7	
1161	B2 V	24950	A	4.40	108	111	1.26	4.02	9.4	16.5	
1162	A0 II	–	–	–	–	–	3.31	–	–	–	
1163	B1 V	27300	A	4.20	301	305	3.52	4.10	11.0	9.9	
1164	B3 V	21500	E	4.00	190	217	1.86	3.87	8.2	24.5	
1165	B1.5 V	26100	A	4.25	184	199	7.02	4.06	10.3	13.4	
1166	B1-3e	24950	IM	4.20	328	302	7.70	4.01	9.8	14.6	

continued on next page

Table A.2. *continued*

Star	Spectral Type	T _{eff} (K)	Method	log <i>g</i> (dex)	<i>v</i> _e sin <i>i</i>		<i>r</i> (′)	log L (L _⊙)	Mass (M _⊙)	Age (Myr)	Comment
					PF (km s ⁻¹)	FT (km s ⁻¹)					
1167	B1.5 V	26100	A	4.05	117	119	2.75	4.05	10.0	13.9	
1168	B9 II	–	–	–	–	–	6.20	–	–	–	
1169	B9 II	–	–	–	–	–	9.83	–	–	–	
1170	B0.5 V	29500	He+	4.35	147	151	3.76	4.17	12.0	7.2	
1171	A2 III-II	–	–	–	–	–	7.21	–	–	–	
1172	B3 V	21500	E	4.15	137	142	7.62	3.86	8.0	25.4	SB1
1173	B1 V	27300	A	4.20	75	72	4.20	4.08	10.6	11.7	
1174	B1-3e	24950	IM	3.40	529	531	6.47	4.00	10.2	14.2	
1175	B2 V	24950	A	4.40	103	96	8.37	3.99	9.4	16.6	
1176	B1.5 V	26100	A	4.35	≤ 40	≤ 40	7.29	4.03	9.8	14.6	
1177	B1-3e	24950	IM	4.05	44	58	6.93	3.99	9.4	16.8	
1178	B1.5 V	26100	A	4.10	88	87	7.50	4.03	9.8	14.1	
1179	B1.5 V	26100	A	4.20	133	134	4.63	4.03	10.0	13.8	
1180	B0.5 V	30000	He+	4.25	166	160	7.90	4.17	12.2	5.9	
1181	B1 V	27300	A	4.10	167	161	2.08	4.07	10.6	11.1	SB1
1182	B0.5 V	29650	A	4.40	195	219	6.40	4.16	12.2	6.2	SB1
1183	B2.5 V	23900	E	4.35	51	≤ 40	9.04	3.93	8.8	19.9	
1184	B1-3 V	24950	I	4.25	183	199	5.34	3.98	9.6	15.5	
1185	B0 V	30500	He+	4.35	170	170	0.86	4.19	12.6	4.9	
1186	B2 V	24950	A	4.05	41	41	4.09	3.98	9.4	16.3	
1187	B5e	–	–	–	212	234	2.92	–	–	–	
1188	B1-2 V	26100	I	4.15	310	294	3.15	4.01	10.2	12.1	SB1
1189	B1 V	27300	A	4.15	227	215	2.11	4.06	10.6	10.6	
1190	B1-3e	24950	IM	4.00	278	284	5.38	3.96	9.6	14.7	
1191	B1.5 V	26100	A	4.25	106	93	2.96	4.01	10.2	12.1	SB1
1192	B2 V	24950	A	4.20	128	123	8.34	3.97	9.2	16.5	SB1
1193	B1-2e	26100	IM	3.70	326	304	7.65	4.01	10.2	12.0	
1194	B3e	21500	EM	3.80	204	196	1.91	3.82	7.8	25.3	
1195	B1.5 V	26100	A	4.40	104	114	3.62	4.01	9.8	13.9	
1196	B1 V	29500	He+	4.40	141	136	7.02	4.13	11.8	6.6	SB1
1197	B1.5 V	26100	A	4.05	147	140	3.42	4.01	9.8	13.7	
1198	B1.5 V	26000	He+	3.80	47	46	4.46	4.00	9.8	14.2	
1199	B0 V	34750	He+	4.40	≤ 40	≤ 40	0.94	4.32	15.6	0.0	
1200	B1 V	27300	A	4.10	≤ 40	≤ 40	6.74	4.04	10.2	11.9	
1201	B2.5 V	23900	E	4.35	92	105	4.00	3.91	8.8	19.3	
1202	A0 II	–	–	–	–	–	7.65	–	–	–	
1203	B2-3e (shell)	23900	EM	3.95	327	298	8.78	3.90	9.0	17.0	
1204	A3 III	–	–	–	–	–	2.77	–	–	–	
1205	B2.5 V	23900	E	4.10	107	108	7.94	3.89	8.6	19.3	
1206	B2.5 V	23900	E	4.20	42	46	3.88	3.89	8.6	19.3	
1207	B3 V	21500	E	4.25	≤ 40	≤ 40	5.60	3.79	7.6	27.2	
1208	B2.5 V	23900	E	4.05	114	128	7.04	3.89	8.6	19.1	
1209	B3 V	21500	E	3.85	132	145	6.04	3.78	7.6	26.4	SB1
1210	B3e (shell)	21500	EM	3.40	234	238	6.83	3.78	7.8	25.2	
1211	B1.5 V	26100	A	4.20	241	243	4.55	3.97	9.8	12.4	
1212	B3e	21500	EM	4.15	300	307	3.30	3.78	8.0	24.0	
1213	B1-3e	24950	IM	4.00	309	304	6.87	3.92	9.4	14.3	
1214	B1-3e	24950	IM	3.90	351	336	4.96	3.92	9.4	14.3	
1215	B3 III	18450	A	3.45	96	87	8.25	3.62	6.4	41.2	
1216	B1.5 V	26100	A	4.15	251	272	2.13	3.95	9.8	11.9	
1217	B2.5 V	23900	E	4.15	≤ 40	≤ 40	5.90	3.86	8.4	20.0	
1218	B2.5 V	23900	E	3.85	266	266	6.35	3.86	8.8	17.4	
1219	B1.5 V	26100	A	4.30	83	99	4.57	3.95	9.6	13.6	
1220	B1.5 V	26100	A	4.20	160	155	2.27	3.95	9.6	13.2	
1221	B0.5 V	29200	Si	4.25	≤ 40	≤ 40	2.81	4.06	11.2	6.8	
1222	B1 V	27300	A	4.30	259	265	3.97	3.98	10.4	8.9	
1223	B1 V	27300	A	4.30	47	55	6.29	3.98	10.2	10.8	

continued on next page

Table A.2. *continued*

Star	Spectral Type	T _{eff} (K)	Method	log <i>g</i> (dex)	<i>v</i> _e sin <i>i</i>		<i>r</i> (′)	log L (L _⊙)	Mass (M _⊙)	Age (Myr)	Comment
					PF (km s ⁻¹)	FT					
1224	B1-2e	26100	IM	4.00	247	238	7.43	3.94	9.8	12.2	
1225	B3 V	21500	E	4.20	96	79	5.84	3.75	7.4	27.4	
1226	B1.5 V	26100	A	4.15	94	99	6.62	3.94	9.6	13.6	
1227	B3 V	21500	E	4.05	54	68	8.54	3.75	7.4	27.5	
1228	B9 II	–	–	–	–	–	9.15	–	–	–	
1229	B1.5 V	26100	A	4.30	194	212	4.78	3.93	9.6	12.3	
1230	B0.5 V	29650	A	4.25	199	198	3.74	4.06	11.8	3.9	
1231	B8 II	12500	He	3.15	66	79	2.26	3.19	–	–	
1232	B1 V	27300	A	4.45	149	135	0.55	3.97	10.2	10.1	
1233	B0.2 V	30650	Si	4.40	≤ 40	≤ 40	3.22	4.10	12.0	3.0	
1234	B2.5 V	23900	E	4.00	≤ 40	≤ 40	2.92	3.84	8.4	20.0	
1235	B3 V	21500	E	4.15	236	213	5.46	3.74	7.6	25.9	
1236	B1 V	27000	He+	4.30	69	67	1.17	3.96	10.2	9.0	
1237	B3e	21500	EM	4.00	200	220	8.63	3.74	7.6	25.9	
1238	B2.5 V	23900	E	3.90	135	141	5.62	3.84	8.4	19.0	
1239	B2 V	24950	A	4.35	44	41	7.37	3.88	8.8	16.8	
1240	B3 V	21500	E	3.70	272	262	6.49	3.73	7.6	25.2	
1241	B1 V	27300	A	4.35	94	99	2.31	3.96	10.2	10.1	SB1
1242	B2 V	24950	A	4.50	280	298	6.11	3.87	9.2	13.9	
1243	B3 V	21500	E	4.15	65	70	4.02	3.73	7.4	27.8	
1244	B2.5 V	23900	E	3.95	120	135	1.53	3.82	8.4	19.1	
1245	B1.5 V	26100	A	4.15	148	133	6.41	3.91	9.4	13.0	
1246	B3 V	21500	E	4.10	131	119	6.33	3.72	7.4	27.4	SB1
1247	B1.5 V	26100	A	4.20	188	187	0.39	3.90	9.6	12.3	

Appendix B: Comments on individual targets

#1001 – MPG 435: This is the visually brightest object in the main body of NGC 346, first observed spectroscopically by Walborn (1978, his ‘NGC 346 No. 1’) and classified as O4 III(n)(f). From consideration of its absolute magnitude, and from the offset of the stellar radial velocities compared to the nebular emission features, Niemela et al. (1986) suggested it as a likely binary. Indeed, Niemela (2002) reported radial velocity variations in the system (classifying the spectra as O4f+O:), with a refined estimate of the period of 24.2 d given by Niemela & Gamen (2004). The FLAMES data, observed as part of the Field A configuration, also reveal a massive companion. Note that this is probably not related to the multiple components reported by Heydari-Malayeri & Hutsemekers (1991), which are at distances of greater than 1''5 (thus outside the Medusa fibre diameter).

The $\lambda\lambda 4450\text{--}4565$ region of #1001 is shown for our two LR02 spectra in Fig. B.1. Double components are clearly seen in the data from 2004 September 27, whereas the observation from the following night merely shows line asymmetry – such a rapid change for a relatively long-period system is consistent with the eccentric orbit ($e = 0.42 \pm 0.04$) from Niemela & Gamen (2004). For completeness we also include a previously unpublished spectrum of the system from the University College London Echelle Spectrograph (UCLES) on the Anglo Australian Telescope (AAT), contemporary to those presented by Walborn et al. (2000) – similar evidence of multiplicity is also seen.

NIV $\lambda 4058$ emission (requiring a spectral type of O4 or earlier) is seen in the LR02 spectra at a velocity consistent with the blueward component in Fig. B.1. The presence of He I $\lambda 4471$ absorption, combined with weak He II $\lambda 4686$ emission (albeit complicated by absorption from the secondary) suggests a classification for the primary of O4 If. The He I $\lambda 4471$ absorption for the secondary is also weaker than that for He II $\lambda 4542$ (Fig. B.1), suggesting a classification of O5-6.

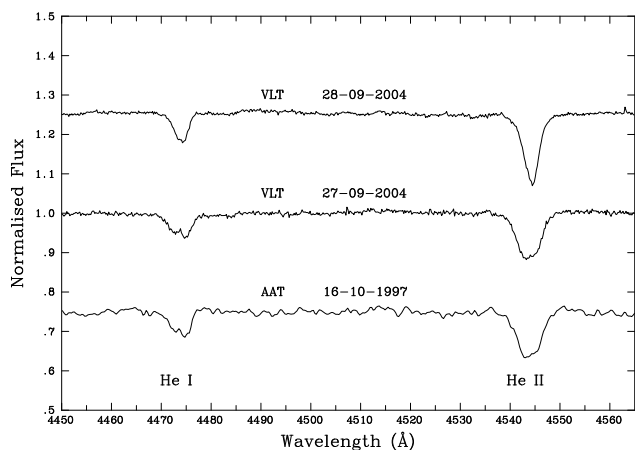


Fig. B.1. #1001 – MPG 435: Multiple components are seen in the FLAMES spectra. Evidence for multiplicity is also seen in an unpublished AAT-UCLES spectrum (degraded and binned to the same resolution as the FLAMES data).

#1010 – MPG 342: Niemela et al. (1986) also suggested this star as a likely binary, with further monitoring by Massey et al. (2012) revealing a third component. The FLAMES spectra, obtained in the Field B configuration, are best described as O5-6 V((f)), but the multiplicity complicates precise classification and prompted us to re-inspect another unpublished AAT-UCLES spectrum (again contemporary to those from Walborn et al.

2000) which also shows evidence of three components (see Fig. B.2).

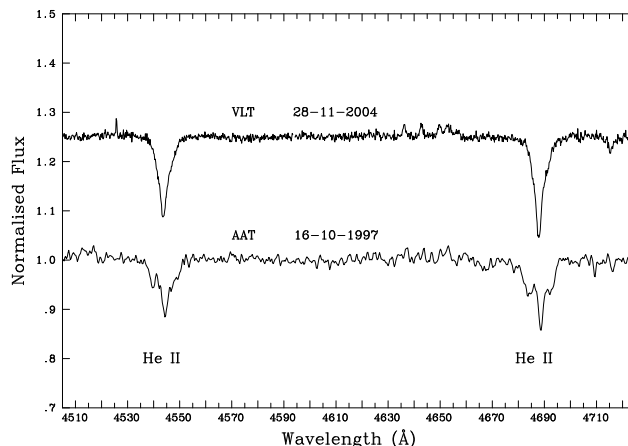


Fig. B.2. #1010 – MPG 342: LR03 FLAMES spectrum in which #1010 appears single, compared with a previously unpublished AAT-UCLES spectrum (degraded/binned to the FLAMES resolution), in which three components appear to be present.

#1012 – MPG 368: As one of the brightest stars in the cluster, #1012 has been observed by a number of authors. Classifications of O5-6: V, O5.5 V((f+)), O4-5 V((f)) and O6 V were given by Niemela et al. (1986), Massey et al. (1989), Walborn et al. (2000), and Massey et al. (2009), respectively. Massey et al. reported a velocity difference (50 km s^{-1}) between the He I and He II lines in their spectrum of the star and suggested it is a binary, with more recent high-resolution spectroscopy from Bouret et al. (2013) finding evidence of two components in the He I lines. The FLAMES spectra also reveal a velocity shift (of $\sim 50 \text{ km s}^{-1}$) within the observations, providing further support of its binary nature (hence the past uncertainty in its classifications).

#1024 – MPG 665, MA93#1138, KWB346#93: This source was noted as an emission-line object by Meyssonnier & Azzopardi (1993, their #1138) then by Keller et al. (1999, #93) in their search for Be-type stars; on the basis of imaging polarimetry, Wisniewski et al. (2007) argued that it is most likely a classical Be star. However, #1024 was identified by Udalski et al. (1998, SMC_SC8, #160677) as an eclipsing binary system from the second Optical Gravitational Lensing Experiment (OGLE) survey, with a period of 86.4 d, updated to 86.2 d by Wyrzykowski et al. (2004) and then 86.25 d by Pawlak et al. (2013).

Strong twin-peaked emission is seen in $H\beta$, with weak He I absorption combined with a rich metal-line absorption spectrum super-imposed (consistent with a late A spectral type). This initially suggested a Be-type object with a cooler disk. The time-sampling of our data is unfortunately relatively limited (#1024 was observed in Field A), but the LR03 observations were taken three nights apart and variations are seen in the $H\beta$ region (see Fig. B.3). The first observation (2004 Oct 01) has been red-shifted by 15 km s^{-1} such that the metal absorption lines roughly match those in the second observation; note the residual offset in He I $\lambda 4922$ ($\sim 40 \text{ km s}^{-1}$) and shell-like emission in Fe II $\lambda 4923$. Similar behaviour is also seen in He I $\lambda 4713$ and $\lambda 5016$ but the velocity of the $H\beta$ emission appears consistent with the cooler spectrum. The blue:red ratio of the $H\beta$ emission changes, perhaps related to relative shifts in the line profile of the hotter companion rather than arising from the

longer-term changes often seen and thought to arise from disk structure (Hanuschik et al. 1995). This system merits further study to ascertain its evolutionary status, but could be related to the peculiar A-type supergiants reported by Mennickent & Smith (2010).

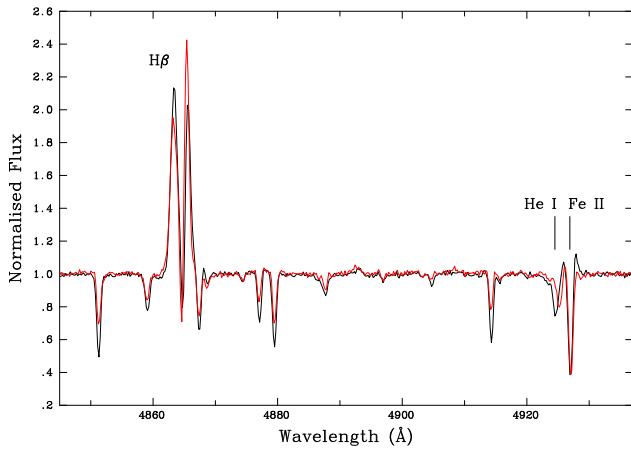


Fig. B.3. Combined LR03 observations for #1024 from the two observational epochs. The spectrum from the first epoch (black line) has been redshifted by 15 km s^{-1} such that the metallic spectra approximately agree – note the offset in the He I $\lambda 4922$ absorption, indicative of a hotter companion, and the shell-like emission of Fe II $\lambda 4923$.

#1030 – MPG 655: The spectrum of #1030 (MPG 655) has very narrow lines, similar to those seen in NGC 346-028 from the FSMS (*aka* MPG 113), classified as OC6 Vz by Walborn et al. (2000). The He I lines suggest a slightly earlier type for #1030, but there is also evidence of nebular infilling, so we classify its spectrum as OC5-6 Vz. From lower-resolution spectroscopy, Heydari-Malayeri & Selier (2010) classified this star as O5 V + OB, with the suggestion of a secondary component arising from the strength of the He I lines given an O5 V classification (Dr. N. R. Walborn, private communication); from our (albeit limited) time coverage, we see no evidence for radial velocity shifts. If the spectrum is convolved by a rotational broadening profile of, for example, 200 km s^{-1} , the He II $\lambda 4686$ line still remains stronger than the other helium lines, suggesting its classification as ‘Vz’ spectrum is not due to either resolution or $v_e \sin i$ effects.